

1 Increasing precipitation due to climate change could partially 2 offset the impact of warming on glacier loss in the monsoon- 3 influenced Himalaya until 2100 CE

4
5 Anya M. Schlich-Davies^{1*}, Ann V. Rowan^{2*}, Andrew N. Ross¹, Duncan J. Quincey³, Vivi K.
6 Pedersen⁴

7
8 ¹Priestley International Centre for Climate, School of Earth and Environment, University of Leeds,
9 UK

10 ²Department of Earth Science, University of Bergen and Bjerknes Centre for Climate Research,
11 Bergen, Norway

12 ³School of Geography, University of Leeds, UK

13 ⁴Department of Geoscience, Aarhus University, Aarhus C, Denmark

14
15 *These authors contributed equally to this work

16
17 Correspondence to: Ann V. Rowan (ann.rowan@uib.no)

18
19
20 **Abstract.** Glacier mass in the Himalaya is projected to shrink by 53–70% due to climate change by
21 2100 CE. However, the impact of changes in precipitation amount and distribution on future glacier
22 change remains uncertain because mesoscale meteorology is not represented in current glacier models.
23 We explored the combined effects of past and future changes in air temperature and precipitation
24 amount and distribution on the evolution of Khumbu Glacier in the Everest region of Nepal. We used a
25 climate-glacier modelling approach that forced an ice-dynamical glacier evolution model with surface
26 mass balance forcings that included mesoscale meteorological variables derived from downscaling of
27 Regional Climate Model results. Our simulations show that historical warming has committed Khumbu
28 Glacier to future mass loss of 10–23% during this century, and that under an intermediate future
29 emissions scenario (RCP4.5), Khumbu Glacier could lose 70% mass by 2100 CE due to warming.
30 However, the projected increase in precipitation in tandem with warming could offset about half of the
31 projected glacier loss, such that the total decrease in glacier mass by 2100 CE compared to the present
32 day would be reduced to 34%. Under a high future emissions scenario (RCP8.5) glacier loss due to
33 warming will not be compensated by changes in precipitation, but will instead result in substantial
34 ablation above 6,000 m with devastating consequences for one of the highest glaciers on Earth.

35 36 1. Introduction

37 Projecting glacier mass change in response to climate change is important for determining the impact
38 of anthropogenic warming on regional water availability (Pritchard, 2019). High Mountain Asia is
39 projected to lose $34 \pm 19\%$ of glacier mass by 2100 CE if warming is limited to 1.5°C to meet the
40 ambitious Paris Agreement target (Kraaijenbrink et al., 2017). Less ambitious projections give $53 \pm$
41 23% glacier mass loss by 2100 CE under the intermediate emissions scenario RCP4.5, and $69 \pm 20\%$
42 under the high emissions scenario RCP8.5 (Kraaijenbrink et al., 2017; Marzeion et al., 2020; Rounce
43 et al., 2023). However, such projections are challenging to make because accumulation and ablation
44 processes in mountain environments are driven by orographic feedbacks between high-relief
45 topography and atmospheric circulation systems such as the South Asian Summer Monsoon
46 (Bookhagen and Burbank, 2006). Furthermore, large uncertainties arise from the challenge of
47 simulating the interactions between the mass balance regimes of monsoon-influenced glaciers, where
48 accumulation and ablation both occur during the monsoon season, and the dynamics of glaciers flowing
49 through high-relief topography that includes processes such as the development of supraglacial debris
50 layers that modify surface melting (Dehecq et al., 2019; Miles et al., 2018b; Salerno et al., 2023).
51 Variability in the extent and intensity of the Indian Summer Monsoon during the Last Glacial Maximum
52 affected glacier expansion in the monsoon-influenced Himalaya through changes in snowfall
53 distribution (Benn and Owen, 1998; Owen et al., 2009). Future Indian Summer Monsoon precipitation

54 and variability projected in Global Circulation Models (GCMs) will increase with current global
55 warming (Katzenberger et al., 2021), but the effect of projected changes in precipitation amount, timing,
56 and phase (rain/snow) on Himalayan glaciers remain poorly constrained (Immerzeel et al., 2012; Mölg
57 et al., 2014; Ragetti et al., 2016; Shaw et al., 2022; Shea et al., 2015).

58
59 Supraglacial debris covers 4–7% of glacier surfaces globally and 30% of glacier ablation areas in the
60 Himalaya, and modifies the response of glaciers to climate change relative to regional trends (Herreid
61 and Pellicciotti, 2020; Kraaijenbrink et al., 2017; Rounce et al., 2023; Rowan et al., 2015). Satellite
62 observations show that the rate of glacier mass loss across the Himalaya has accelerated over the last
63 40 years for both clean-ice glaciers and debris-covered glaciers (Maurer et al., 2019). Observations and
64 modelling studies indicate that thick supraglacial debris caused historical mass loss from debris-covered
65 glaciers to lag that of clean-ice glaciers, such that debris-covered glaciers are currently larger than would
66 otherwise be the case (King et al., 2020; Rounce et al., 2023; Rowan et al., 2021). However, the
67 dampening effect of supraglacial debris on glacier mass loss is overturned by the development of
68 extensive supraglacial ponds and ice cliffs within debris layers (Miles et al., 2018a; Strickland et al.,
69 2023) and the stagnation and detachment of debris-covered tongues from the upper and more active
70 sections of glaciers (Rowan et al., 2021). Quantifying the impact of feedbacks set up by the formation
71 and expansion of supraglacial debris layers at a regional scale requires exploring these processes at
72 scales that can be resolved in ice-dynamical glacier evolution models (Rowan et al., 2015; Nicholson
73 et al., 2021; Compagno et al., 2022). These processes can be considered in 2-D (along the glacier
74 flowline) either considering stochastic debris delivery to the glacier (Vacco et al., 2010; Wirbel et al.,
75 2018) or continuous debris delivery, which can result in the over-accumulation of debris at the terminus
76 (Anderson and Anderson, 2016; Ferguson and Vieli, 2020; Juvet et al., 2011), or in 3-D (using the
77 horizontal and vertical ice flow fields), which allows the lateral transport and deposition of debris to
78 the margins of the ablation area (Rowan et al., 2015).

79
80 While recent rapid warming resulted in a rise in regional equilibrium line altitude (ELA), that caused
81 recession and collapse of glacier termini for both clean-ice glaciers and debris-covered glaciers, the
82 decay of the former ablation areas of debris-covered glaciers is relatively delayed by supraglacial debris,
83 such that the terminus of the actively flowing glacier can remain in contact with the detached ice tongue
84 rather than separating (Maurer et al., 2019; Pellicciotti et al., 2015; Rowan et al., 2021). In common
85 with most large debris-covered Himalayan glaciers, Khumbu Glacier in the Everest region of Nepal is
86 in greater imbalance with climate than a climatically equivalent clean-ice glacier, and has maintained a
87 more extensive ice volume than would be possible without supraglacial debris (Rowan et al., 2021).
88 However, as a result of reduced ice flux from the accumulation area, the debris-covered tongue no
89 longer receives much (or any) input of ice, and has dynamically detached from the active glacier (Fig.
90 1c); this observation is confirmed by the rapid reduction in ice flow and the peak in glacier surface
91 lowering below the Khumbu Icefall where the debris layer is thinnest (King et al., 2020; Quincey et al.,
92 2009). Therefore, the active glacier and the stagnant debris-covered tongue will evolve along different
93 trajectories, and only the part of Khumbu Glacier above the terminus of the active glacier can be
94 considered dynamic (Fig. 1). Projections of future glacier evolution should therefore discount the
95 heavily debris-covered former tongue, which is decaying *in situ* without any input of new ice from the
96 accumulation area, while considering the development of supraglacial debris across the ablation area of
97 the active glacier.

98
99 We applied a novel glacier-climate modelling approach to Khumbu Glacier to test the hypothesis that
100 changes in precipitation in response to climate change will reduce the impact of warming on glacier
101 mass loss. Khumbu Glacier is a benchmark debris-covered glacier in the monsoon-influenced Himalaya
102 flowing from 7,981 m above sea level (a.s.l.) to 4,879 m a.s.l. that is representative of the majority of
103 glaciers in this region (Fig. 1). We used a 3-D ice-flow model forced by mass balance calculated from
104 mesoscale meteorological variables to simulate the evolution of Khumbu Glacier from the late
105 Holocene (~1 ka) through the present day (2015 CE) until 2100 CE using results from three downscaled
106 Regional Climate Models (RCMs) under two Relative Concentration Pathways (RCPs). This approach
107 represents an advance in the use of such models to understand the evolution of Himalayan glaciers; for
108 the first time mesoscale meteorological forcing is used with a climate-glacier model that represents the

109 processes of sublimation, snow avalanching, and debris transport, all of which are important controls
110 on the mass balance of Himalayan glaciers. Simulations start from the late Holocene when Khumbu
111 Glacier was last in dynamic equilibrium with the local climate, as evidenced by large ice-marginal
112 moraines dated to 1.3 ± 0.1 ka surrounding the present-day glacier (Hornsey et al., 2022), and when the
113 glacier surface was free of debris (Rowan et al., 2015). The focus of our experiments is to simulate
114 glacier evolution to the end of the 21st Century. However, the centennial dynamic response time of a
115 large debris-covered glacier such as Khumbu Glacier means that the glacier continues to evolve beyond
116 this time scale, and we continued the simulations until 2300 CE to explore longer-term glacier
117 evolution, albeit with greater uncertainties associated with results beyond 2100 CE.

118

119 **2. Climate-glacier modelling of Khumbu Glacier**

120 The climate-glacier glacier model experiments used mesoscale meteorological variables at an
121 appropriate scale to calculate surface mass balance for the Khumbu Glacier catchment in combination
122 with a debris-covered glacier evolution model to represent the surface processes that modify mass
123 balance. Our approach produced a total of six simulations of Khumbu Glacier from three CORDEX
124 South Asia region RCMs (NOAA, CCCma, IPSL; Lutz et al., 2016) and two RCPs (RCP4.5 and
125 RCP8.5; Collins et al., 2013) to explore the impacts of possible variability in future precipitation amount
126 and distribution in tandem with warming on glacier evolution. Before we use the RCMs to force the
127 future climate scenarios, we evaluated their capabilities against observations of present-day weather
128 and climate. The experimental design represents an advance compared with previous climate-glacier
129 modelling efforts by including robust representations of; (1) mesoscale meteorological phenomena,
130 including sublimation, (2) the redistribution of surface mass balance by snow avalanching, and (3) the
131 feedbacks between debris transport, ice flow and mass balance. This section describes the experimental
132 design for the climate-glacier modelling workflow (Fig. 2); a description of the study site, downscaling
133 of the present-day RCMs using meteorological data from automatic weather stations in the Khumbu
134 Valley, downscaling of the future RCMs for both RCPs, the surface energy and mass balance
135 calculations using COSIPY, and the debris-covered glacier evolution modelling using iSOSIA.

136

137 Khumbu Glacier (RGI2000-v7.0-G-15-08331) is 16.0 km long with an area of 26.4 km². The median
138 glacier elevation is 6,025 m a.s.l. from the terminus at 4,879 m a.s.l. to the headwall at 7,981 m a.s.l.
139 (RGI 7.0 Consortium, 2023). The stagnant debris-covered tongue has an area of 6.2 km² (23% of the
140 total glacier). The ‘Little Ice Age’ (LIA) maximum of Khumbu Glacier occurred about 500 years before
141 present, which is consistent with ages produced for moraines elsewhere in the central Himalaya
142 (Hornsey et al., 2022; Rowan, 2017). Khumbu Glacier was slightly larger than today during the late
143 Holocene, transitioning from a clean-ice glacier with high velocities and efficient export of debris to an
144 debris-covered glacier with lower velocities during the LIA; this change was initiated by the reduction
145 in ice flux promoted by a rise in ELA and thickening supraglacial debris (Rowan et al., 2015).
146 Observations and modelling of the dynamics and structure of Khumbu Glacier show that the lowest five
147 km (25% of the total length, 20% of total ice volume) is stagnant and dynamically detached from the
148 active glacier in the last century (Miles et al., 2021; Quincey et al., 2009; Rowan et al., 2021). Basal ice
149 at the glacier surface indicates that the active terminus overrides the stagnant glacier tongue (Miles et
150 al., 2021) and measurements of surface displacement show no longitudinal flow through the detached
151 debris-covered tongue, which is collapsing laterally at a rate of about 3 m a⁻¹ (Watson et al., 2017).

152

153 **2.1 Glacier-climate model experimental design**

154 As a starting point for our transient simulations of Khumbu Glacier, we reconstructed the late Holocene
155 glacier from an ice-free domain using an ELA of 5,325 m a.s.l. and an atmospheric lapse rate of 4.0°C
156 km⁻¹ in a 5 kyr simulation. The simulation continued through the LIA forced by forced by a step change
157 in mean annual air temperature (MAAT) equivalent to 1.5°C colder than the present day over 500 years
158 following Rowan et al. (2015, 2021). Ice-marginal moraines denoting the late Holocene (1.3 ± 0.1 ka)
159 glacier extent and thickness (Hornsey et al., 2022) were used to constrain the spin-up simulation. The
160 ice-free domain was found by subtracting the estimated ice thickness (Farinotti et al., 2019) from a 30-
161 m digital elevation model (DEM) acquired from the Shuttle Radar Topography Mission (Farr et al.,
162 2007). The ice-free model domain incorporated the full hydrological catchment including the steep
163 hillslopes in the Western Cwm that provide snow to the glacier surface by avalanching. We simulated

164 only the active section of the glacier to the present day and future, and assigned the detached debris-
165 covered tongue to the model domain as a static topographic feature. The late Holocene spin-up
166 simulation was forced to present-day conditions using three surface mass balances (one from each
167 RCM) calculated using the Coupled Snowpack and Ice-surface Energy and Mass Balance model in
168 Python (COSIPY v1.3) (Sauter et al., 2020). These simulations were evaluated against a range of
169 observations (Fig. 3) and the experiment using the NOAA RCM was identified as the starting point for
170 all future simulations because this was most representative of the observed glacier. For more detail on
171 the glacier model parameterisation and evaluation of the present-day simulation using geological and
172 remote sensing observations, we refer to Rowan et al. (2021).

173
174 The simulations continued from the present day to 2100 CE forced by the distributed glacier surface
175 mass balances calculated for each of the three RCMs and two RCPs using COSIPY. The three RCMs
176 and two future RCPs represent a range of possible future climates including distinctly different
177 precipitation trends, equivalent to dry, moderate and wet scenarios under warming of 1.4–2.2°C under
178 RCP4.5 and 3.8–4.1°C under RCP8.5 (Table 1; Section 2.2). We used climate time slices representing
179 the present day (2015–2020 CE) and the end of the 21st Century (2095–2100 CE) to calculate surface
180 mass balance. The five-year time slices were chosen to reduce the computational expense of the
181 modelling (~24 hours per simulation), and the preceding decade was used to evaluate these time slices
182 (Section 3.3). We used a step forcing rather than interpolating mass balance over time, whereby the
183 future mass balance was imposed and the glacier adjusted to this from the start of the century in
184 question. Thus we arrived at the present-day simulation from the LIA simulation by forcing the LIA
185 glacier with the 2015–2020 CE mass balance for 200 years. We use the output from the present-day
186 simulation with the 2095–2100 CE mass balance to force the model to 2100 CE for a period of 80 years.
187 We then use the result from this simulation as the starting point for the 2200 CE simulation forced by
188 the 2195–2200 CE mass balance for 100 years, and the same approach for the 2300 CE using the 2295–
189 2300 CE mass balance. Beyond 2100 CE less detailed climate projections are available; given the
190 absence of regional climate projections, globally projected temperature changes were used to extend
191 the end-of-century mass balances. These gave a further increase in temperature of 0.5°C by 2200 CE
192 and 0.7°C by 2300 CE under RCP4.5, and 2.8°C by 2200 CE and 4.1°C by 2300 CE under RCP8.5
193 (Table 1; Collins et al., 2013). No precipitation changes were applied to the post-2100 CE climates due
194 to the absence of projections for precipitation in the CORDEX RCMs and the high uncertainties
195 associated with projections of global precipitation changes for this period.

196
197 We tested a range of lapse rates from 3.0°C km⁻¹ to 6.0°C km⁻¹ based on the range of monthly values
198 calculated from regression of NASA MODIS land surface temperature data for the Central Himalaya
199 while maintaining the same ELA, which resulted in a difference in ice volume of 0.4 x 10⁹ m³ and no
200 change in glacier length at the present day. We examined the uncertainty in accumulation resulting from
201 the application of a calculation to move snowfall from slopes susceptible to avalanching. Observations
202 of high-elevation Himalayan glaciers, including Khumbu Glacier, indicate that up to 75% of
203 accumulation occurs by avalanching rather than direct snowfall (Benn and Lehmkuhl, 2000).
204 Avalanching affects Khumbu Glacier in two ways; by moving snow from steep hillslopes onto the
205 glacier surface thus increasing accumulation from that calculated from direct snowfall onto the glacier
206 surface, and by redistributing snow across steep sections of the glacier surface. If avalanching was not
207 considered in the glacier model then accumulation of snow calculated using COSIPY within the
208 catchment but outside the glacier outline would have no impact on mass balance, resulting in an
209 underestimation of ice volume. When avalanching was not simulated, accumulation occurred at a
210 uniform rate of 2.0 w.e. m a⁻¹ across the Western Cwm, and the resulting glacier had a similar extent
211 but a volume more than double that of the glacier simulated with avalanche redistribution of snow,
212 because mass was not redistributed effectively across steep sections of the glacier surface.

213 214 **2.2 Present-day RCM downscaling using meteorological observations**

215 Six RCMs were assessed on their fidelity to present-day climate using hindcasting (Biemans et al.,
216 2013) with emphasis on temperature seasonality and seasonal precipitation dynamics, given the
217 importance of these variables for glacier mass balance. RCMs from the Coordinated Regional
218 Downscaling Experiment (CORDEX) South Asia domain dynamically downscaled from CMIP5 GCMs

219 by the Indian Institute of Tropical Meteorology to a 50 km spatial resolution (Lutz et al., 2016) were
220 downloaded for the grid box containing Khumbu Glacier (27.9065056°N, 86.4352951°E). Three of the
221 six CORDEX South Asia RCMs (NOAA, CCCma, IPSL) spanning a range of possible future
222 precipitation conditions (Table 1) were selected as discrete scenarios for the glacier surface energy and
223 mass balance calculations. The three remaining RCMs were discounted due to being intermediate to
224 those selected for our experiments (i.e. close to the future precipitation scenario represented by CCCma)
225 or particularly poor at reproducing seasonal temperature and precipitation cycles. For example, despite
226 the annual precipitation sums from the CSIRO RCM being closest to observed values and having the
227 potential to be the ‘driest’ scenario examined, analysis of precipitation seasonality indicated that the
228 monsoon signal was completely absent, with this RCM instead showing a strong dominance of winter
229 precipitation.

230
231 The present-day RCM results were downscaled using quantile mapping, also known as “distribution
232 mapping”, using 14 years of observations from three automatic weather stations (AWS; Fig. 1c and
233 Appendix A) collected between January 2006 and November 2019 with gaps filled using interpolated
234 data from neighbouring stations if required (Fig. 2). Parametric quantile mapping (Piani et al., 2010)
235 was used, whereby a statistical relationship between the raw climate model outputs and observations
236 was formed by substituting the RCM results with observations at a cumulative density function of the
237 prescribed distribution (e.g., a gaussian distribution for temperature; Luo et al., 2018; a gamma
238 distribution for precipitation; Piani et al., 2010). This correction was applied to the raw RCM outputs
239 to produce a third downscaled dataset with an improved the fit to the observations (Maraun et al., 2016).
240 The quantile mapping approach was chosen because this is effective for downscaling precipitation and
241 reduces errors in the standard deviation, the coefficient of variation, and the skewness of distributed
242 values relative to other methods (Lafon et al., 2013; Reiter et al., 2018). The AWS data were also used
243 to disaggregate the resultant daily downscaled present-day and end-of-century climate model outputs
244 to an hourly resolution for energy balance modelling. All meteorological variables, excluding
245 precipitation, were downscaled using the MELODIST Python tool (Förster et al., 2016). Seasonal
246 means were applied for precipitation to reproduce the ‘nocturnal peak’ seen during the monsoon that
247 MELODIST was unable to replicate. Further information on RCM downscaling and AWS data analysis
248 are provided in Appendix A.

249 **2.3 Future RCM downscaling**

250
251 Two future emission scenarios (RCP4.5 and RCP8.5) were available from CORDEX South Asia, which
252 represent only intermediate and high emissions by 2100 CE relative to the present day. These two
253 emissions scenarios are frequently used in climate impact studies enabling the comparison of our results
254 with studies that use other climate/glacier model projections. The two future emissions scenarios were
255 analysed for each of the three CORDEX RCMs to account for the inherently high uncertainties in future
256 precipitation trends associated with climate models and the interplay of changing precipitation with
257 atmospheric warming. The same statistical downscaling approach and disaggregation used for the three
258 present-day RCMs (described in Section 2.2) was applied to the raw CORDEX RCM daily outputs for
259 the three future RCM time slices under RCP4.5 and RCP8.5. The temperature change between the
260 present day and the future time slices was preserved and there was no evidence of any imposed
261 strengthening in the monsoon resulting from this downscaling. An increase in the frequency of days per
262 year outside of the monsoon season with high precipitation amounts (defined here as over 15 mm of
263 daily precipitation) accounted in large part for the higher annual precipitation amounts relative to the
264 present day that were found in four out of the six RCMs. However, the total future annual precipitation
265 increase was on average 8.8% greater in the downscaled climates relative to the raw RCMs, suggesting
266 that this positive trend was inflated by downscaling. The downscaled climates reduced the frequency
267 of precipitation, although, as in present day observations, monsoon precipitation occurred frequently
268 and could be characterised as predominantly drizzle in the future.

269 **2.4 COSIPY surface energy balance modelling**

270
271 COSIPY is a glacier surface energy and mass balance model that integrates a surface energy and mass
272 balance model with a multi-layer snow and ice model (Weidemann et al., 2018; Sauter et al., 2020).
273 COSIPY was chosen as it is currently considered a leading open-source method for estimating glacier

274 mass balance and has previously been applied to glaciers in High Mountain Asia. COSIPY includes a
 275 calculation of sublimation, which is an important ablation process for high-elevation glaciers because
 276 ablation can still occur if the latent heat flux is negative through sublimation, even in instances where
 277 surface temperature and/or air temperature are well below the melting point (Bonekamp et al., 2021;
 278 Brun et al., 2023; Huintjes et al., 2015). COSIPY integrates a surface energy balance model with a
 279 multi-layer snow and ice model and thereby resolves all energy fluxes (F) at the ice surface that
 280 contribute to surface melt (Q_{melt}):

$$281 \quad F = SW_{in} \cdot (1 - \alpha) + LW_{in} + LW_{out} + Q_{sens} + Q_{lat} + Q_g + Q_{liq} \quad \text{Eq.(1)}$$

282
 283 Where SW_{in} is incoming shortwave radiation, α is albedo, LW_{in} and LW_{out} are incoming and outgoing
 284 longwave radiation, and Q_{sens} , Q_{lat} , and Q_g are the sensible, latent, and ground heat fluxes (Oerlemans
 285 et al., 2001) and Q_{liq} is the heat flux from liquid precipitation; the latter variable is often neglected
 286 in ablation calculations (Cuffey and Paterson, 2010) but is of particular importance here as the Indian
 287 Summer Monsoon brings a significant amount of liquid precipitation to the lower reaches of Khumbu
 288 Glacier. The resulting F is equal to the energy available for surface melt (Q_{melt}) when surface
 289 temperature (T_s) is at melting point (0°C). T_s is used to calculate LW_{out} , Q_{sens} , Q_{lat} , Q_g and to partition
 290 solid and liquid precipitation. When T_s exceeds the melting point it is reset to 0°C (273.15 K) and the
 291 residual F fluxes equal Q_{melt} . In this instance, subsurface melt is triggered when the energy fluxes, for
 292 example, penetrating SW_{in} warm the ice layer so that T_s exceeds the melting point of ice (Sauter et al.,
 293 2020).
 294

295
 296 The COSIPY model domain was taken from the 30-m DEM that was resampled to 200-m grid spacing
 297 following sensitivity analyses that revealed minimal impact on the results whilst greatly reducing
 298 computational expense (Fig. 4). CORDEX RCM daily climate variables (temperature, precipitation, the
 299 radiation components, wind speed, relative humidity and atmospheric pressure) were used to force
 300 COSIPY. Snowfall measurements can be used as an input to COSIPY, but precipitation was partitioned
 301 into rainfall and snowfall using the snow transfer scheme within COSIPY given the paucity of
 302 observations and high uncertainties associated with AWS observations, climate reanalysis, and
 303 modelled snowfall products for this region (Sauter et al., 2020). COSIPY was forced using hourly
 304 meteorology with nine variables to calculate the energy balance and mass balance components at an
 305 hourly time step from the sum of accumulation by solid precipitation, deposition, and refreezing of melt
 306 water percolation, and ablation by melt and sublimation. The exchange processes at the surface,
 307 including energy release and consumption with phase changes, control temperature distribution and
 308 phase changes within the glacier (comprised of horizontal ice and snow layers). The coupling of the
 309 surface energy balance component with a multi-layer subsurface snow and ice model accounts for
 310 meltwater refreeze and percolation with the meltwater produced from the surface melt calculations
 311 acting as an input. The mass balance was calculated at an hourly resolution, with accumulation resulting
 312 from the accumulation of solid precipitation on the ice surface, refreeze of meltwater, and deposition
 313 of water vapour, and ablation resulting from subsurface and surface melt and sublimation (Sauter et al.,
 314 2020). The impacts of supraglacial debris on ablation and of snow avalanching on accumulation were
 315 handled in the glacier model.
 316

317 **2.5 Glacier evolution modelling**

318 The second-order shallow ice approximation model (iSOSIA) is a 3-D higher-order ice-dynamical
 319 glacier evolution model that solves for the flow of ice including longitudinal and transverse stress
 320 gradients that are imposed on ice flow through high-relief topography (Egholm et al., 2011). This glacier
 321 model simulates the evolution of debris-covered glaciers by incorporating the feedbacks between debris
 322 transport, mass balance and ice flow (Rowan et al., 2015) and includes two processes that are important
 323 for many Himalayan glaciers—the redistribution of snow by avalanching that is estimated to account
 324 for 75% of accumulation, and the formation of a supraglacial debris layer that insulates the ice surface
 325 to modify ablation (Rowan et al., 2015). While previous versions of this glacier model used depth-
 326 integrated ice flow, this version simulates the evolution of Khumbu Glacier in 3-D as the ice thickness
 327 is divided into 20 vertical layers to calculate englacial debris transport (Rowan et al., 2015). The glacier

328 model has a variable time step that can adjust up to a maximum of 0.1 years to allow greater
329 computational efficiency.

330

331 The distributed surface mass balances calculated using COSIPY using the downscaled RCMs for the
332 periods 2015–2020 CE and 2095–2100 CE were used as inputs to the glacier model with no change in
333 forcing applied between time steps. Surface processes within the glacier model modified the distribution
334 of accumulation and ablation but this was not updated into the surface topography used in COSIPY.
335 Simulated accumulation was the result of the total snowfall in each cell and avalanching of snow
336 imposed for the accumulated snowpack from hillslopes by removing snow and ice from hillslopes
337 greater than 28° and redistributing this mass across less steep surfaces using a non-linear hillslope flux
338 model (Roering et al., 1999). The avalanching routine was found to be sufficient to prevent snow and
339 ice accumulation on slopes that are observed to be free of glacier ice such as the southwest face of
340 Sagarmatha (Mt. Everest) while allowing accumulation on steep sections of the glacier (Rowan et al.,
341 2015) resulting in accumulation rates at the glacier surface in line with the limited available
342 observations for Himalayan glaciers of 2 m water equivalent (w.e.) per year (Benn and Lehmkuhl,
343 2000).

344

345 Rock avalanching is responsible for much of the debris accumulation on the glacier surface but there is
346 little information about the magnitude and frequency of these events, so headwall erosion was assumed
347 to be uniform at 1 mm a⁻¹ (Rowan et al., 2021). Debris produced by headwall erosion was delivered to
348 the glacier surface using a similar non-linear hillslope flux model to snow avalanching. The reduction
349 in ablation beneath supraglacial debris from clean-ice values was represented as a reciprocal function
350 that scaled clean-ice ablation (b_{clean}) to give sub-debris melt (b_{debris}) as a function of debris thickness
351 (h):

352

$$353 \quad b_{debris} = b_{clean} \times \frac{h_0}{h + h_0} \quad \text{Eq. (2)}$$

354

355 where h_0 is a constant representing the characteristic debris thickness at which the reduction in ablation
356 due to insulation by supraglacial debris is 50% of the value for an equivalent clean-ice surface
357 (Anderson and Anderson, 2016; Rowan et al., 2021). The observed heterogeneity of surface ablation
358 required a parameterisation of sub-debris melt representing the effects of differential ablation, which
359 was represented in Equation (2) using a value for h_0 of 0.8 m (Bartlett et al., 2021; Rowan et al., 2021;
360 Strickland et al., 2023).

361

362 **3. Results**

363 **3.1 COSIPY parameter perturbations**

364 The sensitivity of glacier mass balance to individual meteorological variables (MAAT, radiative fluxes,
365 relative humidity, lapse rate, precipitation amount, precipitation phase, glacier surface roughness) was
366 calculated in experiments that perturbed these variables individually. Perturbations were made within
367 the range of the possible uncertainties for each variable that arise from a combination of the choice of
368 observations or climate models, the downscaling approach used, and the distribution of meteorological
369 variables. The values used for perturbations of MAAT and precipitation amount were similar to those
370 expected for possible future climate forcings.

371

372 The spatially averaged mass balance was most sensitive to changes in MAAT (perturbed by ±1.5°C,
373 2.0°C and 3.0°C), $LWin$ and $SWin$ (±10% and 20%). Perturbations of relative humidity (±10% and 20%)
374 had the least impact on mass balance. The use of a seasonal lapse rate of 5.38°C km⁻¹ yielded a spatially
375 averaged mass balance that was 5.6% less than the reference calculation value, while a diurnal lapse
376 rate gave a mass balance that was only 0.45% lower because the reference lapse rate was close to the
377 mean of the day/night lapse rates, whereas the environmental lapse rate (6.50°C km⁻¹) gave a mass
378 balance that was 1.24% higher than the reference value. The relatively small difference in mass balance
379 due to the choice of lapse rate is due to the extremely high elevation of Khumbu Glacier, which means
380 that MAAT is below 0°C in the accumulation area for much of the year and a higher lapse rate does not
381 affect rain/snow partitioning. The largest difference in mass balance due to the choice of lapse rate was

382 of $\pm 24\%$ just below the ELA. The installation of the National Geographic automatic weather stations
383 on Mt. Everest in 2019 provided an opportunity to examine lapse rates at the highest elevations. For the
384 period April–November 2019, the observed lapse rate was $4.68^\circ\text{C km}^{-1}$ between Phortse (3,810 m a.s.l.)
385 and Everest Base Camp (5,315 m. a.s.l.) and $5.36^\circ\text{C km}^{-1}$ between Camp II and South Col, similar to
386 the value used in this study. The lapse rate above 8,000 m a.s.l. was about $1.2^\circ\text{C km}^{-1}$ greater than that
387 below 5,600 m a.s.l. between the two highest AWS (South Col and Balcony) indicating that in the
388 highest-elevation sections of the catchment, lapse rates may be best represented by values considered
389 suitable for the free atmosphere. The glacier ice surface roughness (z_0) value was 1.7 mm (Table 2),
390 which is a reasonable estimate for clean-ice glaciers (Mölg et al., 2012). The z_0 values reported in the
391 existing literature vary widely even for clean-ice glaciers and do not consider debris-covered glacier
392 surfaces, and so two substantially different z_0 values were tested as endmembers of the likely range in
393 z_0 values; 0.1 mm from Midtre Lovénbreen in Svalbard (Irvine-Fynn et al., 2014) and August-One
394 Glacier in China (Guo et al., 2018), and 6.9 mm for the clean-ice section of Haut Glacier D’Arolla
395 (Brock et al., 2006). Adjusting z_0 had minimal impact on mass balance, although a higher (lower) z_0 did
396 result in slightly increased (decreased) mass balance.

397
398 Coupled parameter testing involved perturbing precipitation and MAAT simultaneously. The most
399 significant change in spatially averaged mass balance followed a 3°C increase in MAAT and 20%
400 decrease in precipitation amount. The change in ablation following an increase in temperature of 1.5°C
401 was compensated by accumulation resulting from 20% higher precipitation. The impact on mass
402 balance of two precipitation phase (rain/snow) partitioning schemes was investigated and compared
403 with the default snow transfer function in COSIPY; (1) using threshold temperatures of 0.5°C , 2.0°C ,
404 and 3.5°C , and (2) using a calculation that smoothly scaled rain/snow partitioning from 100% solid
405 precipitation at -1°C to 0% solid precipitation at 4°C . The height of the 0°C isotherm during months
406 that experienced significant ablation (May–September) fluctuated around 5,125–6,250 m a.s.l., which
407 correlated with the elevations that experienced the greatest mass balance change with lapse rate. While
408 the lapse rate used to distribute MAAT did not have a significant impact on glacier-wide mass balance,
409 the elevation of the 0°C isotherm from the pre-monsoon until the end of the monsoon was sensitive to
410 the air temperature distribution.

411 412 **3.2 Evaluation of COSIPY surface energy and mass balance results**

413 Turbulent fluxes and energy balance components across Khumbu Glacier were explored across a three-
414 year period to assess the performance of COSIPY and understand their relative spatial importance. A
415 reference simulation was made using COSIPY for comparison with observed glacier mass balance and
416 tested across a range of grid spacings (30 m to 1 km). The reference simulation represented the period
417 2013–2015 CE and was forced by AWS data (Appendix A) using the model parameters in Table 2.

418
419 COSIPY was used to calculate clean-ice surface mass balance from the downscaled RCMs, and the
420 insulating effects of supraglacial debris were calculated in the glacier model. The glacier-wide clean-
421 ice mass balance for the three-year reference period was -3.4 m w.e, which equates to -1.13 m w.e a^{-1} .
422 Maximum ablation was up to 16.2 m w.e. over three years (Fig. 4). High precipitation events were
423 observed to offset some ablation if they occurred outside the core monsoon season (e.g., in October
424 2013 and May 2014) but did not influence monsoon season ablation when high air temperatures and
425 strong incoming radiative fluxes rapidly remove snow cover and drive melting. Higher minimum
426 temperatures in winter 2013–2014 CE relative to the other winters did not significantly influence
427 accumulation rates, which remained similar to those in 2014–2015 CE. Low precipitation amounts
428 during the 2015 monsoon (286 mm in 2015, compared to 330.8 mm in 2013, and 333.9 mm in 2014)
429 resulted in lower accumulation in the upper reaches of the glacier. The precipitation gradient was
430 calibrated to $1 \times 10^{-5} \% \text{ m}^{-1}$ to match observed accumulation rates. However, this gradient largely arises
431 from avalanching (Benn and Lehmkuhl, 2000) which is challenging to represent in COSIPY and was
432 instead handled in the glacier model (Section 2.5).

433
434 The energy available for ablation peaked in the pre-monsoon and monsoon, bringing higher rates of
435 sublimation and subsurface melt in April–June (Fig. 5). Simulated sublimation occurred at all
436 elevations, with the highest cumulative loss near the South Col (EB7910) where sublimation dominated

437 mass balance and only slightly slowed from December until May. Sublimation rates were increasingly
438 tied to seasonality with distance down-glacier, with rates on the lower section of the tongue (EB4980)
439 increasing from April until the start of the monsoon in July. Calculated subsurface melt was negligible
440 at or above the ELA (5,950 m a.s.l.) whereas at lower elevations sub-surface melt dominated mass
441 balance with a stronger seasonal cycle related to surface temperature. The interannual variability in
442 subsurface melt was linked to surface temperature, although low simulated subsurface melt rates in the
443 first year of the reference simulation were largely due to persistence of the initial snow cover that
444 shielded the subsurface from surface temperature until the subsurface adapted to local conditions.
445 Refreezing occurred across the entire glacier, with a staggered onset due to increased elevation, and the
446 absolute values were low. The higher latent heat flux during the monsoon resulted in higher deposition
447 of snow to the glacier at the lower elevations, with negligible rates at higher elevation. Similar absolute
448 values and patterns are seen for condensation.

449
450 Calculated incoming shortwave radiation matched well with observations from Ev-K2-CNR,
451 GlacioClim, and high-elevation AWS networks (Matthews et al., 2020) indicating that the radiation
452 model in COSIPY performed well across the extreme relief of the Khumbu Glacier catchment (Fig. 6).
453 Net shortwave radiation contributed the largest energy input to the glacier surface at lower elevations,
454 correlating most strongly with the energy available for melt with a mean correlation coefficient of 0.79.
455 There was high temporal variability related to variable cloud cover exhibited in the hourly incoming
456 shortwave radiation forcing and fluctuating albedo during the warmer months with the melting of the
457 snowpack. The high incoming shortwave radiation the upper reaches of the glacier indicate that low net
458 shortwave radiation is not due to topographic shading. Net shortwave radiation was correlated with
459 albedo ($r = 0.86$), and the persistence of snow throughout much of the year reduced the energy available
460 for melt. Net longwave radiation also contributed to the energy available for melt as the pattern of both
461 fluxes corresponded. Between 5,900–7,900 m a.s.l., net longwave radiation sometimes exceeded zero
462 during the monsoon, most likely due to heavy cloud cover and increased temperatures relative to the
463 glacier surface. The latent heat flux was almost zero at the lower elevation sites as the arrival of the
464 monsoon resulted in higher relative humidity, and this pattern was similar, but dampened, at higher
465 elevation. At the South Col (EB7910) the energy available for melt correlated exactly ($r = 1$) with the
466 sensible heat flux (Fig. 6).

467
468 Grid spacings for the climate-glacier model of 30 m, 50 m, 200 m and 1 km were tested to ensure that
469 that the COSIPY calculations captured orographic effects without unnecessary computational expense.
470 The simulated maximum accumulation rate did not change significantly with grid spacing, giving
471 accumulation rates of 2.1–3.9 m w.e. at 6,500–7,000 m a.s.l. in the reference simulation. The 1 km grid
472 spacing contained only 27 glacier points, and gave a similar spatial mean mass balance to the finer-
473 resolution calculations (Fig. 4), but there were large gaps in mass balance calculated across the glacier
474 that affected the height of the ELA and significantly reduced the calculated maximum accumulation
475 value. The 30-m and 50-m grid spacings captured greater spatial variability in mass balance relative to
476 the 200 m resolution calculation, particularly at elevations between 5200–5400 m a.s.l.. However, as
477 the ELA, and the calculated maximum and minimum mass balances were not significantly different
478 between these finer-resolution calculations, the 200 m grid spacing was used throughout to benefit from
479 the much reduced computational expense.

480 481 **3.3 Evaluation of the RCM downscaling**

482 The downscaled climate variables from the three RCMs for the present-day time slices (2015–2020 CE)
483 were evaluated against 14 years of observations from three AWS to assess the representation of means,
484 seasonality, diurnal cycles, day-to-day variability, and interannual variability. All three downscaled
485 RCMs showed good agreement between mean annual air temperature ($-2.15 \pm 0.05^\circ\text{C}$) and observed
486 air temperature from the Pyramid AWS (Appendix A). The representation of the monsoon was greatly
487 improved by the RCM downscaling; temperature seasonality was well resolved following quantile
488 mapping and the monthly mean and minimum air temperatures were similar to observations across the
489 present-day time slices (Fig. A1). The monsoon stabilised air temperatures and reduced the range
490 between minimum and maximum temperatures in the downscaled RCMs, which was in better
491 agreement with AWS observations, but was not present in the raw RCMs prior to downscaling. We note

492 that the downscaled maximum air temperature was at times higher than observations amongst all RCMs
493 during the post-monsoon and winter (Fig. A1), but that the distribution of downscaled air temperatures
494 was similar to observed values (Fig. A2). Gamma distribution quantile mapping substantially improved
495 the absolute precipitation values relative to the AWS observations compared to those in the raw RCMs;
496 the overestimation of winter precipitation and relative underestimation of monsoon precipitation
497 amounts in the raw RCMs was reduced and downscaled results show a clearer monsoon signal (Fig.
498 A3). When compared with AWS observations, RCM downscaling slightly over-corrected the seasonal
499 precipitation pattern with a slight underestimation of winter precipitation for the most extreme winter
500 events. Across the three present-day simulations, the surface mass balance calculated using the NOAA
501 RCM was more positive than for the ISPL and CCCma RCMs and most similar to the mass balance
502 calculated from meteorological observations.
503

504 **3.4 Evaluation of the glacier model results**

505 The simulated glacier geometry and dynamics (Fig. 7) were compared with remotely sensed
506 observations of velocity, surface elevation change, and debris cover extent for the present-day glacier.
507 The distributed surface mass balances calculated using COSIPY were most similar to observed values
508 after the calculated surface mass balances were integrated with the glacier model to include
509 accumulation by snow avalanching and the reduction in surface melting beneath supraglacial debris;
510 the glacier extent was underestimated if supraglacial debris is not simulated (Fig. 8). The supraglacial
511 debris-mass balance feedback in the glacier model reproduced the observed reversed mass balance
512 gradient and peak in ablation below the Khumbu Icefall (Fig. 1). The simulated glacier area was 7.8
513 km² and similar to that obtained from structural mapping in 1979 CE (Nakawo, 1986). Radio-echo
514 sounding in 1999 CE obtained ice thickness estimates close to the active terminus of ~160 m (Gades et
515 al., 2000) and simulated ice thickness at the terminus was 130 m. The simulated thickness at the active
516 glacier terminus thickness was approximately 175 m in 1999 CE, which agreed well with observations
517 from DEMs of difference that show thinning here of up to 55 m between 1984–2018 CE (King et al.,
518 2020). Simulated surface elevation change in the ablation area was –30 m over 20 years to the present
519 day and similar to values derived from satellite observations for 1984–2015 CE (King et al., 2020).
520 Simulated present-day glacier velocities (Fig. 9) show a similar pattern and magnitude to glacier surface
521 velocities observed using remote sensing observations, which reach a maximum of 220 m a⁻¹ in the
522 Khumbu Icefall (Altena and Kääb, 2020) and up to 20 m a⁻¹ in the ablation area (Quincey et al., 2009;
523 Dehecq et al. 2019). The simulated present-day velocities in this study were a better fit to remote sensing
524 observations than those from previous simulations that used an elevation-dependent mass balance
525 forcing (Rowan et al., 2015, 2021) where the maximum simulated velocities were 118 m a⁻¹.
526

527 **3.5 Climate change and glacier evolution from the present day until 2100 CE**

528 Khumbu Glacier is responding to historical climate change and will continue to shrink even if warming
529 ceases today. Indeed, if we allow the spin-up experiment to reach equilibrium with the present-day
530 NOAA RCM mass balance, the glacier terminus will recede by 2.1 km and the maximum ice thickness
531 will decrease from 246 m to 206 m by 2100 CE without any additional warming (Fig. 10a). In this
532 simulation, a supraglacial debris layer up to 1.3 m thick extends 1 km up-glacier from the terminus and
533 partially dampens the committed volume loss by sustaining 13% more ice volume than would be the
534 possible for a clean-ice glacier surface with the same mass balance. The committed glacier volume loss
535 due to historical warming in the absence of any further climate forcing is 10–23% of the present-day
536 glacier mass (Fig. 9b) with the associated uncertainty represented by this range of values arising from
537 the parameterisation of the impact of supraglacial debris evolution on surface melting.
538

539 Now considering the effects of additional warming under the RCP scenarios for the NOAA experiment,
540 we find that greater warming occurs in winter than in summer under both RCPs (Sanjay et al., 2017)
541 and results in an increase in annual precipitation amount of about 15% made up of a greater increase in
542 winter precipitation than summer precipitation. The climate forcing from the downscaled NOAA RCM
543 under RCP4.5 is 1.4°C warmer than the present day (–0.75°C in 2095–2100 CE compared with –2.15°C
544 in 2015–2020 CE) and annual precipitation increases by 14.8% from 581.4 mm at present day to 664.8
545 mm a⁻¹ by 2100 CE with summer (June–September) precipitation increasing by 5.4% and winter
546 (December–February) precipitation increasing by 14.1% (Fig. 2). Under RCP8.5, the downscaled

547 climate forcing is projected to be 3.8°C warmer than present day (1.65°C in 2095–2100 CE) with an
548 increase in annual precipitation of 14.9% by 2100 CE, with summer precipitation increasing by 9.8%
549 and winter precipitation increasing by 19.4%. In the NOAA RCM RCP4.5 experiment, the spatially
550 averaged cumulative glacier mass balance is $-0.14 \text{ m w.e. a}^{-1}$ in 2100 CE, which is slightly more
551 positive than the present-day value of $-0.21 \text{ m w.e. a}^{-1}$. Glacier volume decreases by 36% between the
552 present day and 2100 CE (Fig. 10). While significant, this end-of-century glacier loss is partially offset
553 by the concurrent increase in precipitation. In comparison, an equivalent simulation forced only by
554 warming and without any change in precipitation results in a more linear trajectory of glacier change
555 and 70% loss of glacier volume by 2100 CE (light blue line in Fig. 10d) demonstrating that 34% of
556 potential glacier loss from warming could be compensated by the increase in precipitation that occurs
557 as a result of warming.
558

559 The CCCma and IPSL RCMs projected greater warming from the present day by 2100 CE than the
560 NOAA RCM under RCP4.5 with a value of 1.6°C (+0.2°C compared with the NOAA RCM) in the IPSL
561 RCM experiment and 2.2°C (+0.8°C) in the CCCma RCM experiment. These two RCMs also projected
562 slightly greater warming by 2100 CE under RCP8.5, with a value of 3.9°C (+0.1°C compared with the
563 NOAA RCM) for the IPSL RCM experiment and 4.1°C (+0.3°C) for the CCCma RCM experiment. The
564 projected increase in precipitation amount across the three RCMs is similar between RCPs with annual
565 totals above 600 mm by 2100 CE. The CCCma RCM gives the greatest increase in annual precipitation
566 amount of 100 mm by 2100 CE. There is no evidence of change in the intensity of the Indian Summer
567 Monsoon, as the seasonal split in precipitation remains similar to the present day, but the frequency of
568 days with high precipitation (over 15 mm per day) increases by 2100 CE, giving twice as many days in
569 the NOAA RCM experiment and up to seven times as many days in the IPSL RCM experiment. Under
570 RCP8.5, all experiments showed similar results for mass balance by 2100 CE with only a 10%
571 difference in glacier volume between the three RCMs (Fig. 10d). The CCCma RCM experiment has
572 only a 1% difference in volume loss between RCP4.5 and RCP8.5 by 2100 CE despite a 1.9°C
573 difference in MAAT—this is a surprising result given the significant temperature difference, which can
574 be attributed to the greater number of high-magnitude precipitation events that occur under RCP8.5 in
575 combination with the small difference in winter temperatures between the two RCPs. Indeed, in the
576 CCCma RCM experiment under RCP4.5, the maximum winter temperature is 1.7°C higher than for the
577 other RCMs, resulting in ablation and rainfall (rather than snowfall) during the winter.
578

579 **3.6 Climate change and glacier evolution from 2100 CE until 2300 CE**

580 Projections of climate change beyond 2100 CE are more uncertain than those for this century and the
581 uncertainties associated with the model experimental design become larger, but these results do indicate
582 a future trajectory for Khumbu Glacier. As there are no regional temperature projections beyond 2100
583 CE we used global values to continue the simulations into the next century (Table 1). However, there
584 are no global projections of precipitation beyond 2100 CE and to avoid introducing potentially
585 significant uncertainties to our results by estimating these values, no changes in precipitation were
586 applied beyond 2100 CE.
587

588 In all the RCP4.5 experiments, there is little change in glacier volume between 2200 CE and 2300 CE
589 compared with 2100 CE regardless of the RCM forcing used (Table 1 and Fig. 10b). In the NOAA
590 RCP4.5 experiment, the Khumbu Icefall is maintained until 2300 CE and ice continues to flow from
591 the Western Cwm to below 6,000 m so that the glacier remains in contact with the dynamically detached
592 tongue. Therefore, keeping warming within the limit of RCP4.5 could restrict future volume loss to
593 only 26% beyond that already committed to by historical climate change, and Khumbu Glacier would
594 reach a new dynamic equilibrium that maintains a sufficient ice thickness to survive for at least two
595 centuries. However, in all the RCP8.5 experiments, substantial glacier loss occurs after 2100 CE and
596 Khumbu Glacier completely decays before 2300 CE.
597

598 Physical detachment of the debris-covered tongue from the active glacier, whereby this area contained
599 no active glacier ice, occurs around 2140 CE in the NOAA experiment (Fig. 9) and around 2070 CE in
600 the CCCma and IPSL experiments. We defined the glacier to be stagnant when the maximum rate of
601 ice flow is less than 10 m a^{-1} ; a conservative estimate of the uncertainty associated with observations

602 of glacier velocities (Dehecq et al., 2019). Accordingly, we consider Khumbu Glacier to no longer be a
603 viable glacier system at the point where there is no ice flow above this value in the entire glacier since
604 there is minimal throughput of ice mass. In the NOAA RCP8.5 experiment, the glacier area is 1.2 km²
605 and the mean velocity reduces to 10 m a⁻¹ by 2260 CE, such that the glacier is no longer viable. Glacier
606 breakdown occurs earlier for the CCCma and IPSL RCM experiments (Fig. 10b) by 2170–2180 CE
607 because loss of ice volume due to warming is not compensated to the same magnitude by the increase
608 in precipitation projected under RCP8.5 in the NOAA RCM experiment.

609

610 **4. Discussion**

611 **4.1 Uncertainties associated with the climate-glacier modelling approach**

612 Sources of uncertainty in our results arose from each step of our climate-glacier modelling workflow,
613 and we considered how the experiments could be designed to reduce these uncertainties. In this section
614 we discuss the potential sources of uncertainty associated with the choice of RCMs, the downscaling
615 of the RCMs, the use of time slices rather than continuous mass balance calculations, the representation
616 of future precipitation in the RCMs, the use of GCM forcing beyond 2100 CE, and the representation
617 of avalanching in the glacier model.

618

619 A single RCM was not considered sufficient to represent both present-day climate and potential future
620 climatic extremes, but the climate-mass balance forcing ensemble was limited in size due to the small
621 number of RCMs available. The use of three RCMs allowed the implications of uncertainties in
622 understanding of local climate for glacier evolution to be evaluated. A multi-model mean approach
623 using all the CORDEX South Asia RCMs (widely used elsewhere) was not considered sufficient to
624 represent present-day and future climate conditions in the Khumbu Valley, as this approach gives equal
625 weighting to models irrespective of their performance (Pierce et al., 2009) and does not enable
626 intercomparison of results for future climate conditions. Five-year downscaled RCM time slices were
627 chosen to reduce computational expense associated with COSIPY and the integration with the glacier
628 model. To ensure that the five-year periods selected were representative, the preceding decade was used
629 for comparison with the time-slice results (Appendix A). The use of quantile mapping with 14 years of
630 AWS data as the downscaling method limited the influence of any natural variability by ensuring that
631 the period did not reflect an extreme phase of natural climate oscillation. This comparison was
632 particularly important for the future time slices, where large uncertainties arise between RCMs and
633 observational data cannot be used for evaluation of the downscaled climate or the resulting mass
634 balance.

635

636 The time slice approach resulted in a stepped response in terms of ice volume change over time where
637 the forcing was changed (Fig. 10d). The glacier continued to evolve through each century rather than
638 equilibrate with the mass balance forcing, but we note that this stepped approach could be improved by
639 interpolating the mass balance over time and coupling the COSIPY and iSOSIA models such that mass
640 balance was calculated dynamically for the evolving ice surface; however this was beyond the scope of
641 our experiments. The experiments were repeated using mid-century (2045–2050 CE) mass balance
642 forcings to simulate glacier evolution until 2100 CE to investigate if this produced a different end-of-
643 century result. These experiments produced near-identical results in 2100 CE to the experiments with
644 no mid-century forcing, because the response time of the simulated glaciers was longer than the 40-
645 year period between the present-day and future time slices. Thus, a mid-century surface mass balance
646 forcing was not considered necessary in our experiments and instead we used a step forcing for mass
647 balance rather than interpolation between mass balance calculations in the glacier model. The
648 reacceleration in glacier mass loss after 2100 CE was in part due to the stepped forcing approach and
649 the uncertainties associated with GCM projections, which increase with time after 2100 CE particularly
650 under RCP8.5. For example, forecasts of global warming for 2281–2300 CE relative to 1986–2005 CE
651 under RCP8.5 range from 3.0°C to 12.6°C (Collins et al., 2013).

652

653 The differences in simulated glacier change and response time that resulted from the RCMs were at
654 times greater than those resulting from the RCPs due to differences in projections of precipitation.
655 Whilst the three selected RCMs performed relatively well in representing annual precipitation cycles
656 from the six available CORDEX RCMs, we note that this representation was still fairly poor, although

657 substantially improved by quantile mapping. The poor representation of monsoon dynamics in the
658 present-day RCMs highlights an additional uncertainty associated with future precipitation scenarios
659 and that these results should be treated as a set of possible scenarios. The CORDEX CMIP5 and CMIP6
660 projects only produced dynamically downscaled RCMs for two future emissions scenarios (RCP4.5 and
661 RCP8.5) and as such the implications of other RCPs for glacier evolution could not be assessed. The
662 downscaled future climates were compared with those from other studies using CORDEX results, and
663 showed similar annual and seasonal regional temperature trends strongly linked to the choice of RCP,
664 and similar positive precipitation trends with poor agreement between RCMs (Kaini et al., 2019; Sanjay
665 et al., 2017). The relationship between precipitation and warming in the two future emissions scenarios
666 was less clear than that for air temperatures because the monsoon-influenced Himalaya has particularly
667 poor RCM consensus and high levels of uncertainty in future precipitation trends with warming relative
668 to other regions in High Mountain Asia (Sanjay et al., 2017). The transition in the glacier model between
669 the downscaled RCM and the GCM forcing could be improved by homogenising the climate model
670 results across 2090–2100 CE, however, as noted above, the computational expense of forcing COSIPY
671 with downscaled RCM outputs to create inputs to the glacier model required the use of a time-slice
672 approach that was limited to five-year periods, and integration of the RCM results with GCM results
673 was beyond the scope of this study. In the absence of RCMs that can project changes in precipitation
674 after 2100 CE, precipitation was maintained at the same level for the glacier surface energy and mass
675 balance model simulations beyond 2100 CE. The end-of-century precipitation amount is therefore
676 unlikely to be reflective of the more distant future and more realistic precipitation projections are
677 required to explore whether the active glacier can be sustained further into the future or will lose ice
678 more rapidly than is found in this study. However, while future precipitation changes may be important
679 for glacier volume change under RCP4.5, we do not expect a sufficient increase in precipitation beyond
680 2100 CE to compensate for the warming projected under RCP8.5.

681
682 A large uncertainty in the glacier model arose from the parameterisation of avalanching, which resulted
683 in increased accumulation along the glacier surface in the Western Cwm and improved the agreement
684 between simulated and observed accumulation rates and distribution (Benn and Lehmkuhl, 2000).
685 Future work to resolve the impact of low frequency–high magnitude avalanche events on accumulation
686 rates would be useful to refine this calculation but the contribution of avalanches to glacier
687 accumulation over decadal time scales remains challenging to measure. Our study addresses fine-scale
688 temporal (hourly) and spatial (100 m) glacier surface processes, including avalanching and sublimation,
689 that affect glacier surface mass balance across the elevation range of Khumbu Glacier, but further
690 observations of meteorological and glaciological conditions at the highest elevations would be
691 beneficial, and are needed if micro-scale processes are to be included in glacier models (Brun et al.,
692 2023; Khadka et al., 2021; Mölg et al., 2014; Shaw et al., 2022).

693 694 **4.2 Comparison with outcomes under RCP8.5**

695 Current global greenhouse gas emissions are following the trajectory of the intermediate emissions
696 scenario RCP4.5, while the high emissions scenario RCP8.5 could be described as ‘low possibility but
697 high impact’ (Pedersen et al., 2020). However, as represented in the RCMs used in our study, mountain
698 regions are warming more rapidly than the global mean such that a global temperature rise of 1.5°C will
699 lead to 2.1 ± 0.1 °C of warming in High Mountain Asia (Kraaijenbrink et al., 2017; Pepin et al., 2022)
700 although the occurrence of elevation-dependent warming above 5,000 m a.s.l. is debated (Gao et al.,
701 2018). The high temperatures projected under RCP8.5 could potentially be offset partly by increased
702 precipitation, given that high-magnitude precipitation events from winter Westerly disturbances
703 increased by a factor of seven between present day and 2100 CE in the IPSL RCM under RCP8.5.
704 However, we found no evidence of future increases in precipitation offsetting RCP8.5 warming; net
705 glacier mass balance was strongly negative in all RCP8.5 experiments and insufficient to maintain any
706 actively flowing glacier. Under RCP8.5, glacier mass balance in the monsoon-influenced Himalaya may
707 therefore shift from being driven by accumulation during the monsoon to predominantly during winter.
708 Monsoon precipitation would only result in snow accumulation at the very highest elevations and would
709 be insufficient to maintain flowing glaciers. This outcome is avoidable by limiting anthropogenic
710 warming to within RCP4.5, which, due to the associated increase in precipitation, could sustain nearly

711 two thirds of the current glacier volume until 2100 CE and potentially for two centuries further into the
712 future.

713

714 A recent global glacier modelling study forced by an ensemble of 10 GCMs projected mass loss of 64%
715 for Khumbu Glacier by 2100 CE (Rounce et al., 2023). In comparison, our experiments project less
716 severe rates of decline, resulting in 30% less mass loss under the RCP4.5 future climate scenario than
717 in the global study (Fig. 10d). One difference between these results is that rather than using the global
718 glacier inventory outline to define the glacier margins we consider only the actively flowing glacier and
719 so exclude 20% of the starting glacier volume in the detached tongue. We would expect the two sections
720 of the glacier to evolve along different paths; while the active glacier responds to climate change as
721 projected in our experiments, thick supraglacial debris mantling the detached tongue could allow this
722 ice mass to survive and slowly decay *in situ* for many decades beyond the present day. The decay of the
723 detached tongue may however increase due to erosion of the surface by ice cliffs and supraglacial water
724 bodies that are expanding across the former glacier surface (King et al., 2020). Our experiments only
725 consider the rapidly changing active glacier, and we expect that the debris-covered tongue would melt
726 more slowly than projected in the global modelling study, but as we do not consider the stagnant tongue
727 to be part of the present-day glacier the ice volume simulated at the start of our experiments is smaller
728 than that represented by Rounce et al. (2023) and other studies based on the RGI glacier inventory. The
729 dynamically detached debris-covered tongue represents 20% of the present-day glacier volume and
730 contains ice estimated as up to 360 m thick. The mean present-day ablation rate across this section of
731 the glacier simulated in Rowan et al. (2021) is $-0.54 \text{ m w.e. a}^{-1}$ which can be used to estimate the life
732 expectancy of the debris-covered tongue assuming no input of ice from the active glacier and no change
733 in ablation rate due to thickening of supraglacial debris or the development of ice cliffs and supraglacial
734 ponds. While the thickest part of the detached tongue may survive for ~ 600 years, the mean life
735 expectancy of this ice mass is 176 ± 148 years from the present day meaning that the former debris-
736 covered tongue will vanish by 2200 CE.

737

738 **4.3 Impacts of microscale meteorology on glacier change**

739 Sublimation simulated in our study occurred at all elevations with the highest rate of ice loss due to
740 sublimation ($-0.12 \text{ m w.e. a}^{-1}$) in the upper reaches of the Khumbu Glacier catchment near to South Col
741 (about 7,495 m a.s.l.) where sublimation dominated ablation with only minor seasonality. Whilst this
742 amount of ice loss by sublimation is not negligible, it is almost half that found in the point-based
743 calculations after adjusting for the different time periods represented by our studies (Matthews et al.,
744 2020), which is likely due to the assumed uniformity of wind speed across the model domain in
745 COSIPY. Future work to improve the calculation of sublimation in distributed surface mass balance
746 calculations for high-elevation glaciers would be valuable. While we have considered the effects of
747 mesoscale meteorology on glacier mass balance, smaller-scale processes operating close to the land
748 surface could also be important. Katabatic winds were suggested to explain a local 15-year decrease in
749 maximum air temperatures and precipitation over glaciers while minimum air temperatures continued
750 to rise (Salerno et al., 2023). However, the impact of micro-scale near-surface cooling on the duration
751 and extent of mesoscale precipitation and accumulation is likely to be minimal and therefore unlikely
752 to significantly affect glacier-wide mass balance (Mott et al., 2020; Shaw et al., 2024). Observations
753 from an AWS on Khumbu Glacier (6,464 m a.s.l.) indicate that surface energy fluxes may be sufficient
754 to cause non-negligible melting of glacier surfaces despite freezing air temperatures (Matthews et al.,
755 2020). Results from an ice core from South Col Glacier ($>8,000 \text{ m a.s.l.}$) combined with COSIPY
756 experiments suggested that ablation may also take place at even at the highest elevations (Potocki et al.,
757 2022). However, a subsequent study found no evidence of change, and identified large uncertainties
758 associated with simulating mass balance at these extreme elevations where sub-daily air temperature
759 gradients and the duration of snow cover strongly affect ablation and accumulation (Brun et al., 2023).
760 Future work is needed to reduce these uncertainties, as very few observations of accumulation processes
761 and the upper limit of ablation processes exist for high-elevation Himalayan glaciers.

762

763 **4.4 The response of large debris-covered glaciers to climate change**

764 The dynamic response time of large glaciers to climate change is of the order of centuries; for this
765 reason, we start our simulations from the late Holocene ($\sim 1 \text{ ka}$) moraine extent when Khumbu Glacier

766 was last considered dynamically stable (Hornsey et al., 2022; Rowan et al., 2015). The relationship
767 between glacier response time and mass balance becomes less important after 2100 CE when the glacier
768 is so small that ice flow has little impact on glacier volume change. Global and regional glacier
769 modelling studies typically start their simulations in the current century (e.g., 2000–2007 CE in
770 Marzeion et al. (2020); 2015 CE in Rounce et al. (2023)) and a further complication arises from the use
771 of global glacier inventories as a starting point for glacier modelling studies as such inventories cannot
772 capture the current dynamic state of glaciers that are imbalanced, and include all ice-covered areas
773 rather than identifying only actively flowing ice. However, satellite-derived velocity products could be
774 used identify where ice flow within glacier outlines declines to negligible rates (Dehecq et al., 2019).

775
776 The RGI 7.0 inventory for Khumbu Glacier is based on imagery from 1999 CE (RGI 7.0 Consortium,
777 2023) where the detached debris-covered tongue represents 20% of the glacier volume contained within
778 this outline (Fig. 1c). Simulations that integrated the stagnant tongue into the model domain rather than
779 as part of the flowing ice improved the representation of simulated ice flow compared to observed
780 values, supporting our conclusion that the debris-covered tongue has been dynamically detached from
781 the active glacier for 50–100 years (Rowan et al., 2021). Field observations support the concept of
782 active and stagnant sections co-existing in contact with each other as englacial optical televiewing
783 indicated that thrusting occurs at several sites, denoted by skewed internal debris layers and of basal ice
784 that has been thrust to the glacier surface, near to the active glacier terminus (Fig. 1c) from the direction
785 of Khumbu Icefall (Miles et al., 2021). Our simulations show that development of supraglacial debris
786 at the active glacier terminus reduced net volume loss by 13% (Fig. 8). Dynamic detachment of debris-
787 covered tongues could allow these glaciers to move closer to equilibrium with a rapidly changing
788 climate, the local mass balance gradient is a more important control on glacier change for both clean-
789 ice glaciers and debris-covered Himalayan glaciers.

790 791 **5. Conclusions**

792 In the monsoon-influenced Himalaya, 85% of the glacier area is located higher than 5,000 m above sea
793 level and 21% is above 6000 m. Despite these high elevations, Himalayan glaciers are rapidly losing
794 ice in response to recent warming and are projected to shrink by 53% to 70% during this century.
795 However, the impact of future changes in precipitation on glacier loss remains uncertain, because
796 mesoscale meteorology is not often represented in glacier model projections. We explored the effects
797 of future warming in tandem with changes in precipitation by simulating the evolution of Khumbu
798 Glacier in the Everest region of Nepal—a benchmark glacier in the monsoon-influenced Nepal
799 Himalaya—using mesoscale glacier surface energy and mass balance modelling forced by downscaled
800 Regional Climate Model outputs. Historical warming commits Khumbu Glacier to loss of 10–23% of
801 the total ice volume by 2100 CE. While warming due to intermediate future greenhouse gas emissions
802 (RCP4.5) will lead to glacier volume loss of 70% by 2100 CE, the projected concurrent increase in
803 precipitation amount will offset 34% of this and so reduce glacier loss by about a half. However, high
804 future emissions (RCP8.5) will not be compensated by changes in precipitation amount but will instead
805 result in substantial ablation above 6,000 m with devastating consequences for one of the highest
806 glaciers on Earth. Our results indicate that the net mass balance of Khumbu Glacier could be close to
807 zero in 2100 CE under RCP4.5 and therefore, if climate change is limited to this intermediate emissions
808 scenario, Khumbu Glacier will recede to the base of the icefall with insignificant further change in
809 glacier volume beyond this point. In this scenario, Khumbu Glacier has a similar extent in 2100 CE to
810 the active section of the present-day glacier, and represents at least one example of how monsoon-
811 influenced Himalayan glaciers could persist into the future if global efforts are sufficient to mitigate
812 anthropogenic climate change.

813
814
815

816 **Code availability**

817 The COSIPY version 1.3 glacier surface energy and mass balance model is available from the original
818 publication describing this model (Sauter et al., 2020) and Zenodo (Arndt et al., 2020). The iSOSIA
819 version spm-3.3.3r glacier model is available from Zenodo (Rowan and Pedersen, 2024).

820

821 **Data availability**

822 Daily data from the Coordinated Regional Downscaling Experiment (CORDEX) South Asia domain
823 were downloaded from the Indian Institute of Tropical Meteorology website
824 (http://cccr.tropmet.res.in/home/cordexsa_about.jsp) for the grid box nearest to Khumbu Glacier
825 (27.9065°N, 86.4353°E). Incoming shortwave and longwave radiation components were downloaded
826 from the ESGF portal (<https://esgf-ui.ceda.ac.uk/cog/projects/cordex-ceda/>). 14 years of meteorological
827 observations were derived from the two Pyramid AWS at 5,050 m a.s.l. and at 5,035 m a.s.l. (SHARE
828 network Ev-K2-CNR; <https://www.evkc2cnr.org>) and the West Changri Nup glacier AWS at 5,363 m
829 a.s.l. (GlacioClim: <https://glacioclim.osug.fr/>).

830

831 **Author contributions**

832 Conceptualisation: DJQ, ANR, AVR

833 Data curation: ASD, ANR, AVR

834 Formal analysis: ASD, ANR, AVR

835 Funding acquisition: DJQ, ANR, AVR

836 Investigation: ASD

837 Methodology: ASD, ANR, AVR, VKP

838 Project administration: DJQ, ANR

839 Resources: DJQ, ANR

840 Software: AVR, VKP

841 Supervision: DJQ, ANR, AVR

842 Validation: ASD, AVR

843 Visualisation: ASD, AVR

844 Writing – original draft preparation: ASD, AVR, DJQ, ANR, VKP

845 Writing – review and editing: ASD, AVR, DJQ, ANR, VKP

846

847 **Competing interests**

848 The authors declare that they have no conflict of interest.

849

850 **Acknowledgements**

851 Tobias Sauter and Anselm Arndt are thanked for support in using COSIPY. We thank Patrick Wagnon
852 for sharing the Pyramid and Changri Nup Glacier automatic weather station data. We thank David
853 Rounce for sharing global glacier model results for Khumbu Glacier from Rounce et al. (2023). Some
854 of the simulations presented were performed on resources provided by Sigma2, the National
855 Infrastructure for High-Performance Computing and Data Storage in Norway.

856

857 **Financial support**

858 ASD was supported by the Priestley International Centre for Climate at the University of Leeds, and a
859 University of Leeds Anniversary Research Scholarship. AVR was supported by a Royal Society
860 Dorothy Hodgkin Research Fellowship (DHF\R1\201113).

861

862

863 **References**

- 864 Altena, B. and Käab, A.: Ensemble matching of repeat satellite images applied to measure fast-changing
865 ice flow, verified with mountain climber trajectories on Khumbu icefall, Mount Everest, J.
866 Glaciol., 66, 905–915, <https://doi.org/10.1017/jog.2020.66>, 2020.
867 Arndt, A., Sauter, T., Saß, B. (2020). cryotools/cosipy: COSIPY v1.3 – An open-source coupled
868 snowpack and ice surface energy and mass balance model (v1.3). Zenodo.
869 <https://doi.org/10.5281/zenodo.3902191>

- 870 Anderson, L. S. and Anderson, R. S.: Modeling debris-covered glaciers: response to steady debris
871 deposition, *The Cryosphere*, 10, 1105–1124, <https://doi.org/10.5194/tc-10-1105-2016>, 2016.
- 872 Bartlett, O. T., Ng, F. S. L., and Rowan, A. V.: Morphology and evolution of supraglacial hummocks on
873 debris-covered Himalayan glaciers, *Earth Surf. Process. Landforms*, 46, 525–539,
874 <https://doi.org/10.1002/esp.5043>, 2021.
- 875 Benn, D. I. and Lehmkuhl, F.: Mass balance and equilibrium-line altitudes of glaciers in high-mountain
876 environments, *Quaternary International*, 65–66, 15–29, [https://doi.org/10.1016/S1040-6182\(99\)00034-8](https://doi.org/10.1016/S1040-6182(99)00034-8), 2000.
- 877 Benn, D. I. and Owen, L. A.: The role of the Indian summer monsoon and the mid-latitude westerlies
878 in Himalayan glaciation: review and speculative discussion, *Journal of the Geological Society*,
879 155, 353–363, <https://doi.org/10.1144/gsjgs.155.2.0353>, 1998.
- 880 H. Biemans, L.H. Speelman, F. Ludwig, E.J. Moors, A.J. Wiltshire, P. Kumar, D. Gerten, P. Kabat
881 (2013) Future water resources for food production in five South Asian river basins and potential
882 for adaptation—A modeling study, *Science of The Total Environment*,
883 <https://doi.org/10.1016/j.scitotenv.2013.05.092>.
- 884 Bonekamp, P. N. J., Wanders, N., Wiel, K., Lutz, A. F., and Immerzeel, W. W.: Using large ensemble
885 modelling to derive future changes in mountain specific climate indicators in a 2 and 3°C warmer
886 world in High Mountain Asia, *Int J Climatol*, 41, <https://doi.org/10.1002/joc.6742>, 2021.
- 887 Bookhagen, B. and Burbank, D. W.: Topography, relief, and TRMM-derived rainfall variations along
888 the Himalaya, *Geophys. Res. Lett.*, 33, L08405, <https://doi.org/10.1029/2006GL026037>, 2006.
- 889 Brock, B.W., Willis, I.C. and Sharp, M.J., 2006. Measurement and parameterization of aerodynamic
890 roughness length variations at Haut Glacier d’Arolla, Switzerland. *Journal of Glaciology*,
891 52(177), pp.281–297. <https://doi.org/10.3189/172756506781828746>
- 892 Brun, F., King, O., Réveillet, M., Amory, C., Planchot, A., Berthier, E., Dehecq, A., Bolch, T., Fourteau,
893 K., Brondex, J., Dumont, M., Mayer, C., Leinss, S., Hugonnet, R., and Wagnon, P.: Everest South
894 Col Glacier did not thin during the period 1984–2017, *The Cryosphere*, 17, 3251–3268,
895 <https://doi.org/10.5194/tc-17-3251-2023>, 2023.
- 896 Collins, M., Knutti, R., and Arblaster, J.: Long-term Climate Change: Projections, Commitments and
897 Irreversibility. In: *Climate Change 2013: The Physical Science Basis. Contribution of Working
898 Group I to the Fifth Assessment Report of the Intergovernmental Panel on Climate Change*
899 [Stocker, T.F., D. Qin, G.-K. Plattner, M. Tignor, S.K. Allen, J. Boschung, A. Nauels, Y. Xia, V.
900 Bex and P.M. Midgley (eds.)]. Cambridge University Press, Cambridge, United Kingdom and
901 New York, NY, USA., 1–108., 2013.
- 902 Compagno, L., Huss, M., Miles, E. S., McCarthy, M. J., Zekollari, H., Dehecq, A., Pellicciotti, F., and
903 Farinotti, D.: Modelling supraglacial debris-cover evolution from the single-glacier to the
904 regional scale: an application to High Mountain Asia, *The Cryosphere*, 16, 1697–1718,
905 <https://doi.org/10.5194/tc-16-1697-2022>, 2022.
- 906 Cuffey, K.M. and Paterson, W.S.B., 2010. *The physics of glaciers*. Academic Press.
- 907 Dehecq, A., Gourmelen, N., Gardner, A. S., Brun, F., Goldberg, D., Nienow, P. W., Berthier, E., Vincent,
908 C., Wagnon, P., and Trouvé, E.: Twenty-first century glacier slowdown driven by mass loss in
909 High Mountain Asia, *Nature Geosci*, 12, 22–27, <https://doi.org/10.1038/s41561-018-0271-9>,
910 2019.
- 911 Egholm, D. L., Knudsen, M. F., Clark, C. D., and Lesemann, J. E.: Modeling the flow of glaciers in
912 steep terrains: The integrated second-order shallow ice approximation (iSOSIA), *J. Geophys.*
913 *Res.*, 116, <https://doi.org/10.1029/2010JF001900>, 2011.
- 914 Farinotti, D., Huss, M., Fürst, J. J., Landmann, J., Machguth, H., Maussion, F., and Pandit, A.: A
915 consensus estimate for the ice thickness distribution of all glaciers on Earth, *Nat. Geosci.*, 12,
916 168–173, <https://doi.org/10.1038/s41561-019-0300-3>, 2019.
- 917 Farr, T. G., Rosen, P. A., Caro, E., Crippen, R., Duren, R., Hensley, S., Kobrick, M., Paller, M.,
918 Rodriguez, E., Roth, L., Seal, D., Shaffer, S., Shimada, J., Umland, J., Werner, M., Oskin, M.,
919 Burbank, D., and Alsdorf, D.: The Shuttle Radar Topography Mission, *Reviews of Geophysics*,
920 45, 2005RG000183, <https://doi.org/10.1029/2005RG000183>, 2007.
- 921 Ferguson, J. and Vieli, A.: Modelling steady states and the transient response of debris-covered glaciers,
922 *Cryosphere*, <https://doi.org/10.5194/tc-2020-228>, 2020.
- 923

924 Förster, K., Hanzer, F., Winter, B., Marke, T., and Strasser, U.: An open-source MEteoroLOGical
925 observation time series DISaggregation Tool (MELODIST v0.1.1), *Geosci. Model Dev.*, 9, 2315–
926 2333, <https://doi.org/10.5194/gmd-9-2315-2016>, 2016.

927 Gades, A., Conway, H., Nereson, N., Naito, N., and Kadota, T.: Radio echo-sounding through
928 supraglacial debris on Lirung and Khumbu Glaciers, Nepal Himalayas, Debris-Covered Glaciers
929 (Proceedings of a workshop held at Seattle, Washington, USA, September 2000). *IAHS*, 264, 13–
930 22, 2000.

931 Gao, Y., Chen, F., Lettenmaier, D. P., Xu, J., Xiao, L., and Li, X.: Does elevation-dependent warming
932 hold true above 5000 m elevation? Lessons from the Tibetan Plateau, *npj Clim Atmos Sci*, 1, 19,
933 <https://doi.org/10.1038/s41612-018-0030-z>, 2018.

934 Gromke, C., Manes, C., Walter, B., Lehning, M. and Guala, M., 2011. Aerodynamic roughness length
935 of fresh snow. *Boundary-Layer Meteorology*, 141, pp.21-34. [https://doi.org/10.1007/s10546-](https://doi.org/10.1007/s10546-011-9623-3)
936 011-9623-3

937 Guo, S., Chen, R., Liu, G., Han, C., Song, Y., Liu, J., Yang, Y., Liu, Z., Wang, X., Liu, X. and Wang, L.,
938 2018. Simple parameterization of aerodynamic roughness lengths and the turbulent heat fluxes
939 at the top of midlatitude August-One Glacier, Qilian Mountains, China. *Journal of Geophysical*
940 *Research: Atmospheres*, 123(21), pp.12-066. <https://doi.org/10.1029/2018JD028875>

941 Herreid, S. and Pellicciotti, F.: The state of rock debris covering Earth’s glaciers, *Nat. Geosci.*, 13, 621–
942 627, <https://doi.org/10.1038/s41561-020-0615-0>, 2020.

943 Hornsey, J., Rowan, A. V., Kirkbride, M. P., Livingstone, S. J., Fabel, D., Rodes, A., Quincey, D. J.,
944 Hubbard, B., and Jomelli, V.: Be-10 Dating of Ice-Marginal Moraines in the Khumbu Valley,
945 Nepal, Central Himalaya, Reveals the Response of Monsoon-Influenced Glaciers to Holocene
946 Climate Change, *JGR Earth Surface*, 127, <https://doi.org/10.1029/2022JF006645>, 2022.

947 Huintjes, E., Neckel, N., Hochschild, V., and Schneider, C.: Surface energy and mass balance at
948 Purogangri ice cap, central Tibetan Plateau, 2001–2011, *J. Glaciol.*, 61, 1048–1060,
949 <https://doi.org/10.3189/2015JoG15J056>, 2015.

950 Immerzeel, W. W., van Beek, L. P. H., Konz, M., Shrestha, A. B., and Bierkens, M. F. P.: Hydrological
951 response to climate change in a glacierized catchment in the Himalayas, *Climatic Change*, 110,
952 721–736, <https://doi.org/10.1007/s10584-011-0143-4>, 2012.

953 Irvine-Fynn, T.D., Sanz-Ablanedo, E., Rutter, N., Smith, M.W. and Chandler, J.H., 2014. Measuring
954 glacier surface roughness using plot-scale, close-range digital photogrammetry. *Journal of*
955 *Glaciology*, 60(223), pp.957-969. doi:10.3189/2014JoG14J032

956 Jouvét, G., Huss, M., Funk, M., and Blatter, H.: Modelling the retreat of Grosser Aletschgletscher,
957 Switzerland, in a changing climate, *J. Glaciol.*, 57, 1033–1045,
958 <https://doi.org/10.3189/002214311798843359>, 2011.

959 Kaini, S., Nepal, S., Pradhananga, S., Gardner, T. and Sharma, A. K. (2019) Representative general
960 circulation models selection and downscaling of climate data for the transboundary Koshi river
961 basin in China and Nepal. *International Journal of Climatology*, 40(9): 4131-4149. doi:
962 10.1002/joc.6447.

963 Katzenberger, A., Schewe, J., Pongratz, J., and Levermann, A.: Robust increase of Indian monsoon
964 rainfall and its variability under future warming in CMIP6 models, *Earth Syst. Dynam.*, 12, 367–
965 386, <https://doi.org/10.5194/esd-12-367-2021>, 2021.

966 Khadka, A., Matthews, T., Perry, L. B., Koch, I., Wagnon, P., Shrestha, D., Sherpa, T. C., Aryal, D., Tait,
967 A., Sherpa, T. G., Tuladhar, S., Baidya, S. K., Elvin, S., Elmore, A. C., Gajurel, A., and Mayewski,
968 P. A.: Weather On MOUNT EVEREST During The 2019 Summer MONSOON, *Weather*, 76, 205–
969 207, <https://doi.org/10.1002/wea.3931>, 2021.

970 King, O., Bhattacharya, A., Ghuffar, S., Tait, A., Guilford, S., Elmore, A. C., and Bolch, T.: Six Decades
971 of Glacier Mass Changes around Mt. Everest Are Revealed by Historical and Contemporary
972 Images, *One Earth*, 3, 608–620, <https://doi.org/10.1016/j.oneear.2020.10.019>, 2020.

973 Knap, W.H. and Oerlemans, J., 1996. The surface albedo of the Greenland ice sheet: satellite-derived
974 and in situ measurements in the Søndre Strømfjord area during the 1991 melt season. *Journal of*
975 *Glaciology*, 42(141), pp.364-374. doi:10.3189/S0022143000004214

976

- 977 Kraaijenbrink, P. D. A., Bierkens, M. F. P., Lutz, A. F., and Immerzeel, W. W.: Impact of a global
978 temperature rise of 1.5 degrees Celsius on Asia's glaciers, *Nature*, 549, 257–260,
979 <https://doi.org/10.1038/nature23878>, 2017.
- 980 Lafon, T., Dadson, S., Buys, G. and Prudhomme, C., 2013. Bias correction of daily precipitation
981 simulated by a regional climate model: a comparison of methods. *International journal of*
982 *climatology*, 33(6), pp.1367-1381.
- 983 Luo, M., Liu, T., Meng, F., Duan, Y., Frankl, A., Bao, A. and De Maeyer, P. 2018. Comparing bias
984 correction methods used in downscaling precipitation and temperature from regional climate
985 models: A case study from the Kaidu River basin in western China. *Water*. 10(8), pp. 1046.
986 <https://doi.org/10.3390/w10081046>
- 987 Lutz, A.F., Immerzeel, W.W., Kraaijenbrink, P.D., Shrestha, A.B. and Bierkens, M.F., 2016. Climate
988 change impacts on the upper Indus hydrology: sources, shifts and extremes. *PloS one*, 11(11),
989 p.e0165630.
- 990 Marzeion, B., Hock, R., Anderson, B., Bliss, A., Champollion, N., Fujita, K., Huss, M., Immerzeel, W.
991 W., Kraaijenbrink, P., Malles, J., Maussion, F., Radić, V., Rounce, D. R., Sakai, A., Shannon, S.,
992 Van De Wal, R., and Zekollari, H.: Partitioning the Uncertainty of Ensemble Projections of
993 Global Glacier Mass Change, *Earth's Future*, 8, e2019EF001470,
994 <https://doi.org/10.1029/2019EF001470>, 2020.
- 995 Maraun, D., 2016. Bias correcting climate change simulations-a critical review. *Current Climate*
996 *Change Reports*, 2(4), pp.211-220.
- 997 Matthews, T., Perry, L. B., Koch, I., Aryal, D., Khadka, A., Shrestha, D., Abernathy, K., Elmore, A. C.,
998 Seimon, A., Tait, A., Elvin, S., Tuladhar, S., Baidya, S. K., Potocki, M., Birkel, S. D., Kang, S.,
999 Sherpa, T. C., Gajurel, A., and Mayewski, P. A.: Going to Extremes: Installing the World's
1000 Highest Weather Stations on Mount Everest, *Bulletin of the American Meteorological Society*,
1001 101, E1870–E1890, <https://doi.org/10.1175/BAMS-D-19-0198.1>, 2020.
- 1002 Maurer, J. M., Schaefer, J. M., Rupper, S., and Corley, A.: Acceleration of ice loss across the Himalayas
1003 over the past 40 years, *Sci. Adv.*, 5, eaav7266, <https://doi.org/10.1126/sciadv.aav7266>, 2019.
- 1004 Miles, E. S., Willis, I., Buri, P., Steiner, J. F., Arnold, N. S., and Pellicciotti, F.: Surface Pond Energy
1005 Absorption Across Four Himalayan Glaciers Accounts for 1/8 of Total Catchment Ice Loss,
1006 *Geophys. Res. Lett.*, 45, <https://doi.org/10.1029/2018GL079678>, 2018a.
- 1007 Miles, K. E., Hubbard, B., Quincey, D. J., Miles, E. S., Sherpa, T. C., Rowan, A. V., and Doyle, S. H.:
1008 Polythermal structure of a Himalayan debris-covered glacier revealed by borehole thermometry,
1009 *Sci Rep*, 8, 16825, <https://doi.org/10.1038/s41598-018-34327-5>, 2018b.
- 1010 Miles, K. E., Hubbard, B., Miles, E. S., Quincey, D. J., Rowan, A. V., Kirkbride, M., and Hornsey, J.:
1011 Continuous borehole optical televiewing reveals variable englacial debris concentrations at
1012 Khumbu Glacier, Nepal, *Commun Earth Environ*, 2, 12, [https://doi.org/10.1038/s43247-020-](https://doi.org/10.1038/s43247-020-00070-x)
1013 [00070-x](https://doi.org/10.1038/s43247-020-00070-x), 2021.
- 1014 Mölg, T., Maussion, F., Yang, W. and Scherer, D., 2012. The footprint of Asian monsoon dynamics in
1015 the mass and energy balance of a Tibetan glacier. *The Cryosphere*, 6(6), pp.1445-1461.
1016 <https://doi.org/10.5194/tc-6-1445-2012>
- 1017 Mölg, T., Maussion, F., and Scherer, D.: Mid-latitude westerlies as a driver of glacier variability in
1018 monsoonal High Asia, *Nature Clim Change*, 4, 68–73, <https://doi.org/10.1038/nclimate2055>,
1019 2014.
- 1020 Mott, R., Stiperski, I., and Nicholson, L.: Spatio-temporal flow variations driving heat exchange
1021 processes at a mountain glacier, *The Cryosphere*, 14, 4699–4718, [https://doi.org/10.5194/tc-14-](https://doi.org/10.5194/tc-14-4699-2020)
1022 [4699-2020](https://doi.org/10.5194/tc-14-4699-2020), 2020.
- 1023 Nakawo, M.: Processes Which Distribute Supraglacial Debris On The Khumbu Glacier, Nepal
1024 Himalaya, *Annals of Glaciology*, 8, 1986.
- 1025 Nicholson, L., Wirbel, A., Mayer, C., and Lambrecht, A.: The Challenge of Non-Stationary Feedbacks
1026 in Modeling the Response of Debris-Covered Glaciers to Climate Forcing, *Front. Earth Sci.*, 9,
1027 662695, <https://doi.org/10.3389/feart.2021.662695>, 2021.
- 1028 Oerlemans, J., 2001. *Glaciers and climate change*. CRC Press.
- 1029 Owen, L. A., Robinson, R., Benn, D. I., Finkel, R. C., Davis, N. K., Yi, C., Putkonen, J., Li, D., and
1030 Murray, A. S.: Quaternary glaciation of Mount Everest, *Quaternary Science Reviews*, 28, 1412–
1031 1433, <https://doi.org/10.1016/j.quascirev.2009.02.010>, 2009.

- 1032 Pedersen, J. S. T., Van Vuuren, D. P., Aparício, B. A., Swart, R., Gupta, J., and Santos, F. D.: Variability
1033 in historical emissions trends suggests a need for a wide range of global scenarios and regional
1034 analyses, *Commun Earth Environ*, 1, 41, <https://doi.org/10.1038/s43247-020-00045-y>, 2020.
- 1035 Pellicciotti, F., Stephan, C., Miles, E., Herreid, S., Immerzeel, W. W., and Bolch, T.: Mass-balance
1036 changes of the debris-covered glaciers in the Langtang Himal, Nepal, from 1974 to 1999, *J.*
1037 *Glaciol.*, 61, 373–386, <https://doi.org/10.3189/2015JoG13J237>, 2015.
- 1038 Pepin, N. C., Arnone, E., Gobiet, A., Haslinger, K., Kotlarski, S., Notarnicola, C., Palazzi, E., Seibert,
1039 P., Serafin, S., Schöner, W., Terzago, S., Thornton, J. M., Vuille, M., and Adler, C.: Climate
1040 Changes and Their Elevational Patterns in the Mountains of the World, *Reviews of Geophysics*,
1041 60, <https://doi.org/10.1029/2020RG000730>, 2022.
- 1042 Piani, C., Weedon, G.P., Best, M., Gomes, S.M., Viterbo, P., Hagemann, S. and Haerter, J.O., 2010.
1043 Statistical bias correction of global simulated daily precipitation and temperature for the
1044 application of hydrological models. *Journal of hydrology*, 395(3-4), pp.199-215.
1045 <https://doi.org/10.1016/j.jhydrol.2010.10.024>
- 1046 Pierce, D. W., Barnett, T. P., Santer, B. D., and Gleckler, P. J.: Selecting global climate models for
1047 regional climate change studies, *Proc. Natl. Acad. Sci. U.S.A.*, 106, 8441–8446,
1048 <https://doi.org/10.1073/pnas.0900094106>, 2009.
- 1049 Potocki, M., Mayewski, P. A., Matthews, T., Perry, L. B., Schwikowski, M., Tait, A. M., Korotkikh, E.,
1050 Clifford, H., Kang, S., Sherpa, T. C., Singh, P. K., Koch, I., and Birkel, S.: Mt. Everest’s highest
1051 glacier is a sentinel for accelerating ice loss, *npj Clim Atmos Sci*, 5, 7,
1052 <https://doi.org/10.1038/s41612-022-00230-0>, 2022.
- 1053 Pritchard, H. D.: Asia’s shrinking glaciers protect large populations from drought stress, *Nature*, 569,
1054 649–654, <https://doi.org/10.1038/s41586-019-1240-1>, 2019.
- 1055 Quincey, D. J., Luckman, A., and Benn, D.: Quantification of Everest region glacier velocities between
1056 1992 and 2002, using satellite radar interferometry and feature tracking, *J. Glaciol.*, 55, 596–606,
1057 <https://doi.org/10.3189/002214309789470987>, 2009.
- 1058 Ragetti, S., Immerzeel, W. W., and Pellicciotti, F.: Contrasting climate change impact on river flows
1059 from high-altitude catchments in the Himalayan and Andes Mountains, *Proc Natl Acad Sci USA*,
1060 113, 9222–9227, <https://doi.org/10.1073/pnas.1606526113>, 2016.
- 1061 RGI 7.0 Consortium: A Dataset of Global Glacier Outlines, Version 7.0. Boulder, Colorado USA.
1062 NSIDC: National Snow and Ice Data Center, <https://doi.org/10.5067/f6jmovy5navz>, 2023.
- 1063 Reiter, P., Gutjahr, O., Schefczyk, L., Heinemann, G. and Casper, M., 2018. Does applying quantile
1064 mapping to subsamples improve the bias correction of daily precipitation?. *International Journal*
1065 *of Climatology*, 38(4), pp.1623-1633.
- 1066 Roering, J. J., Kirchner, J. W., and Dietrich, W. E.: Evidence for nonlinear, diffusive sediment transport
1067 on hillslopes and implications for landscape morphology, *Water Resources Research*, 35, 853–
1068 870, <https://doi.org/10.1029/1998WR900090>, 1999.
- 1069 Rounce, D. R., Hock, R., Maussion, F., Hugonnet, R., Kochtitzky, W., Huss, M., Berthier, E.,
1070 Brinkerhoff, D., Compagno, L., Copland, L., Farinotti, D., Menounos, B., and McNabb, R. W.:
1071 Global glacier change in the 21st century: Every increase in temperature matters, *Science*, 379,
1072 78–83, <https://doi.org/10.1126/science.abo1324>, 2023.
- 1073 Rowan, A. V.: The ‘Little Ice Age’ in the Himalaya: A review of glacier advance driven by Northern
1074 Hemisphere temperature change, *The Holocene*, 27, 292–308,
1075 <https://doi.org/10.1177/0959683616658530>, 2017.
- 1076 Rowan, A. V., Egholm, D. L., Quincey, D. J., and Glasser, N. F.: Modelling the feedbacks between mass
1077 balance, ice flow and debris transport to predict the response to climate change of debris-covered
1078 glaciers in the Himalaya, *Earth and Planetary Science Letters*, 430, 427–438,
1079 <https://doi.org/10.1016/j.epsl.2015.09.004>, 2015.
- 1080 Rowan, A. V., Egholm, D. L., Quincey, D. J., Hubbard, B., King, O., Miles, E. S., Miles, K. E., and
1081 Hornsey, J.: The Role of Differential Ablation and Dynamic Detachment in Driving Accelerating
1082 Mass Loss From a Debris-Covered Himalayan Glacier, *J. Geophys. Res. Earth Surf.*, 126,
1083 <https://doi.org/10.1029/2020JF005761>, 2021.
- 1084 Rowan, A., & Pedersen, V. K. (2024). *annvrowan/isosia: iSOSIA version used in Schlich-Davies et al.*
1085 *(spm-3.3.3r)*. Zenodo. <https://doi.org/10.5281/zenodo.12666864>

- 1086 Salerno, F., Guyennon, N., Yang, K., Shaw, T. E., Lin, C., Colombo, N., Romano, E., Gruber, S., Bolch,
1087 T., Alessandri, A., Cristofanelli, P., Putero, D., Diolaiuti, G., Tartari, G., Verza, G., Thakuri, S.,
1088 Balsamo, G., Miles, E. S., and Pellicciotti, F.: Local cooling and drying induced by Himalayan
1089 glaciers under global warming, *Nat. Geosci.*, 16, 1120–1127, [https://doi.org/10.1038/s41561-](https://doi.org/10.1038/s41561-023-01331-y)
1090 023-01331-y, 2023.
- 1091 Sanjay, J., Krishnan, R., Shrestha, A. B., Rajbhandari, R., and Ren, G.-Y.: Downscaled climate change
1092 projections for the Hindu Kush Himalayan region using CORDEX South Asia regional climate
1093 models, *Advances in Climate Change Research*, 8, 185–198,
1094 <https://doi.org/10.1016/j.accre.2017.08.003>, 2017.
- 1095 Sauter, T., Arndt, A., and Schneider, C.: COSIPY v1.3 – an open-source coupled snowpack and ice
1096 surface energy and mass balance model, *Geosci. Model Dev.*, 13, 5645–5662,
1097 <https://doi.org/10.5194/gmd-13-5645-2020>, 2020.
- 1098 Shaw, T. E., Miles, E. S., Chen, D., Jouberton, A., Kneib, M., Fugger, S., Ou, T., Lai, H.-W., Fujita, K.,
1099 Yang, W., Fatichi, S., and Pellicciotti, F.: Multi-decadal monsoon characteristics and glacier
1100 response in High Mountain Asia, *Environ. Res. Lett.*, 17, 104001, [https://doi.org/10.1088/1748-](https://doi.org/10.1088/1748-9326/ac9008)
1101 9326/ac9008, 2022.
- 1102 Shaw, T. E., Buri, P., McCarthy, M., Miles, E. S., and Pellicciotti, F.: Local Controls on Near-Surface
1103 Glacier Cooling Under Warm Atmospheric Conditions, *JGR Atmospheres*, 129, e2023JD040214,
1104 <https://doi.org/10.1029/2023JD040214>, 2024.
- 1105 Shea, J. M., Immerzeel, W. W., Wagnon, P., Vincent, C., and Bajracharya, S.: Modelling glacier change
1106 in the Everest region, Nepal Himalaya, *The Cryosphere*, 9, 1105–1128,
1107 <https://doi.org/10.5194/tc-9-1105-2015>, 2015.
- 1108 Sherpa, S. F., Wagnon, P., Brun, F., Berthier, E., Vincent, C., Lejeune, Y., et al. (2017). Contrasted
1109 surface mass balances of debris-free glaciers observed between the southern and the inner parts
1110 of the Everest region (2007–15). *Journal of Glaciology*, 63(240), 637–651.
1111 <https://doi.org/10.1017/jog.2017.30>
- 1112 Strickland, R. M., Covington, M. D., Gulley, J. D., Kayastha, R. B., and Blackstock, J. M.: Englacial
1113 Drainage Drives Positive Feedback Depression Growth on the Debris-Covered Ngozumpa
1114 Glacier, Nepal, *Geophysical Research Letters*, 50, e2023GL104389,
1115 <https://doi.org/10.1029/2023GL104389>, 2023.
- 1116 Vacco, D. A., Alley, R. B., and Pollard, D.: Glacial advance and stagnation caused by rock avalanches,
1117 *Earth and Planetary Science Letters*, 294, 123–130, <https://doi.org/10.1016/j.epsl.2010.03.019>,
1118 2010.
- 1119 Wagnon, P., Lafaysse, M., Lejeune, Y., Maisincho, L., Rojas, M. and Chazarin, J.P., 2009.
1120 Understanding and modeling the physical processes that govern the melting of snow cover in a
1121 tropical mountain environment in Ecuador. *Journal of Geophysical Research: Atmospheres*,
1122 114(D19).
- 1123 Watson, C. S., Quincey, D. J., Smith, M. W., Carrivick, J. L., Rowan, A. V., and James, M. R.:
1124 Quantifying ice cliff evolution with multi-temporal point clouds on the debris-covered Khumbu
1125 Glacier, Nepal, *J. Glaciol.*, 63, 823–837, <https://doi.org/10.1017/jog.2017.47>, 2017.
- 1126 Weidemann, S.S., Sauter, T., Malz, P., Jaña, R., Arigony-Neto, J., Casassa, G. and Schneider, C. (2018).
1127 Glacier Mass Changes of Lake-Terminating Grey and Tyndall Glaciers at the Southern Patagonia
1128 Icefield Derived From Geodetic Observations and Energy and Mass Balance Modeling. *Frontiers*
1129 *in Earth Science*, 6: 81. doi: 10.3389/feart.2018.00081.
- 1130 Wirbel, A., Jarosch, A. H., and Nicholson, L.: Modelling debris transport within glaciers by advection
1131 in a full-Stokes ice flow model, *The Cryosphere*, 12, 189–204, [https://doi.org/10.5194/tc-12-189-](https://doi.org/10.5194/tc-12-189-2018)
1132 2018, 2018.
- 1133 Zekollari, H., Huss, M., Farinotti, D., and Lhermitte, S.: Ice-Dynamical Glacier Evolution Modeling—
1134 A Review, *Reviews of Geophysics*, 60, <https://doi.org/10.1029/2021RG000754>, 2022.
- 1135
- 1136

1137 **Tables and captions**

1138

1139 Table 1. Regional Climate Models (RCMs) chosen for this study and details of the Global Circulation
 1140 Models (GCMs) from which these are derived. The NOAA RCM that was considered most
 1141 representative of conditions in the Everest region. The temperature forcings used to project climate
 1142 change beyond 2100 CE are global values (they are simply included against each of the RCMs for ease
 1143 comparing with 2100 temperature change) and include no change in precipitation after 2100 CE.

1144

1145

CORDEX South Asia regional climate model	Driving CMIP5 global climate model	CMIP5 modelling centre	RCM name in this study	Future precipitation scenario (qualitative)	2100 CE mean temperature change from present day (°C)		2200 CE mean temperature change from 2100 CE (°C)		2300 CE mean temperature change from 2100 CE (°C) /2200CE	
					RCP 4.5	RCP 8.5	RCP 4.5	RCP 8.5	RCP 4.5	RCP 8.5
IITM-RegCM4	NOAA-GFDL-GFDL-ESM2M	National Oceanic and Atmospheric Administration (NOAA), USA	NOAA	Wet	1.4	3.8	0.5	2.8	0.7 /0.2	4.1 /1.3
IITM-RegCM4	CCCma-CanESM2	Canadian Centre for Climate Modelling and Analysis (CCCma), Canada	CCCma	Moderate	2.2	4.1	0.5	2.8	0.7	4.1
IITM-RegCM4	IPSL-CMSA-LR	Institut Pierre-Simon Laplace (IPSL), France	IPSL	Dry	1.6	3.8	0.5	2.8	0.7	4.1

1146

1147

1148 Table 2: Model parameters, where α is albedo (of fresh snow, firn and ice), t^* decay time from snow to
 1149 firn, d^* the constant for the effect of snow depth on albedo, and z_0 surface roughness length. The albedo
 1150 values are widely used within the literature for clean. z_0 values are less well parameterised with high
 1151 spatial variability across glacier surfaces. Testing revealed highest sensitivity of mass balance to
 1152 $\alpha_{\text{freshsnow}}$ relative to the other parameters.

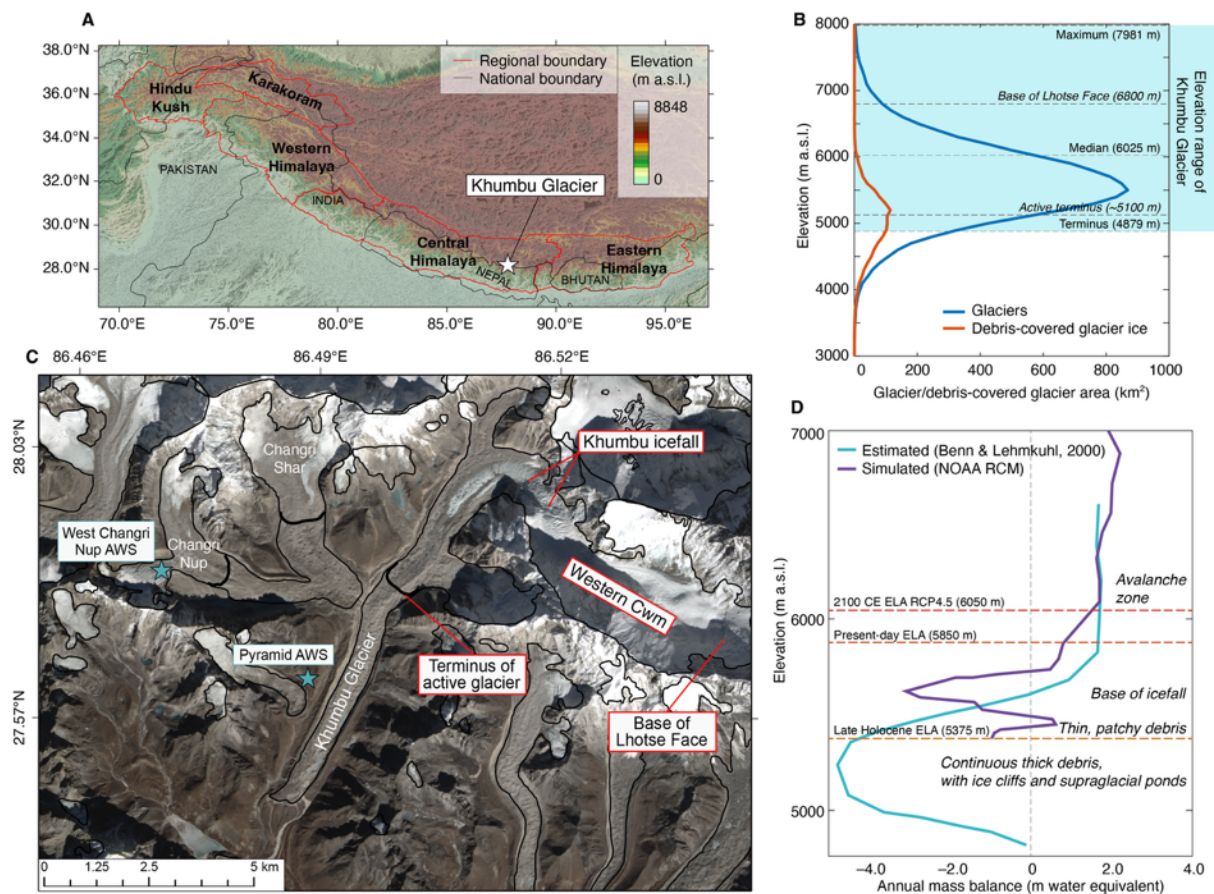
1153

Parameter	Value	Unit	Source
$\alpha_{\text{freshsnow}}$	0.85	-	Mölg et al. 2012; Wagnon et al., 2009
α_{firn}	0.6	-	Knap and Oerlemans, 1996; Mölg et al. 2012
α_{ice}	0.3	-	Mölg et al. 2012
t^*	20	days	Mölg et al. 2012
d^*	1.0	cm	Mölg et al. 2012
$Z_{0\text{snow}}$	0.24	mm	Gromke et al., 2011
$Z_{0\text{firn}}$	4.0	mm	Brock et al., 2006
$Z_{0\text{ice}}$	1.7	mm	Brock et al., 2006
Z_0 ageing length (linearly from $Z_{0\text{snow}}$ to $Z_{0\text{firn}}$)	60	days	Mölg et al. 2012

1154

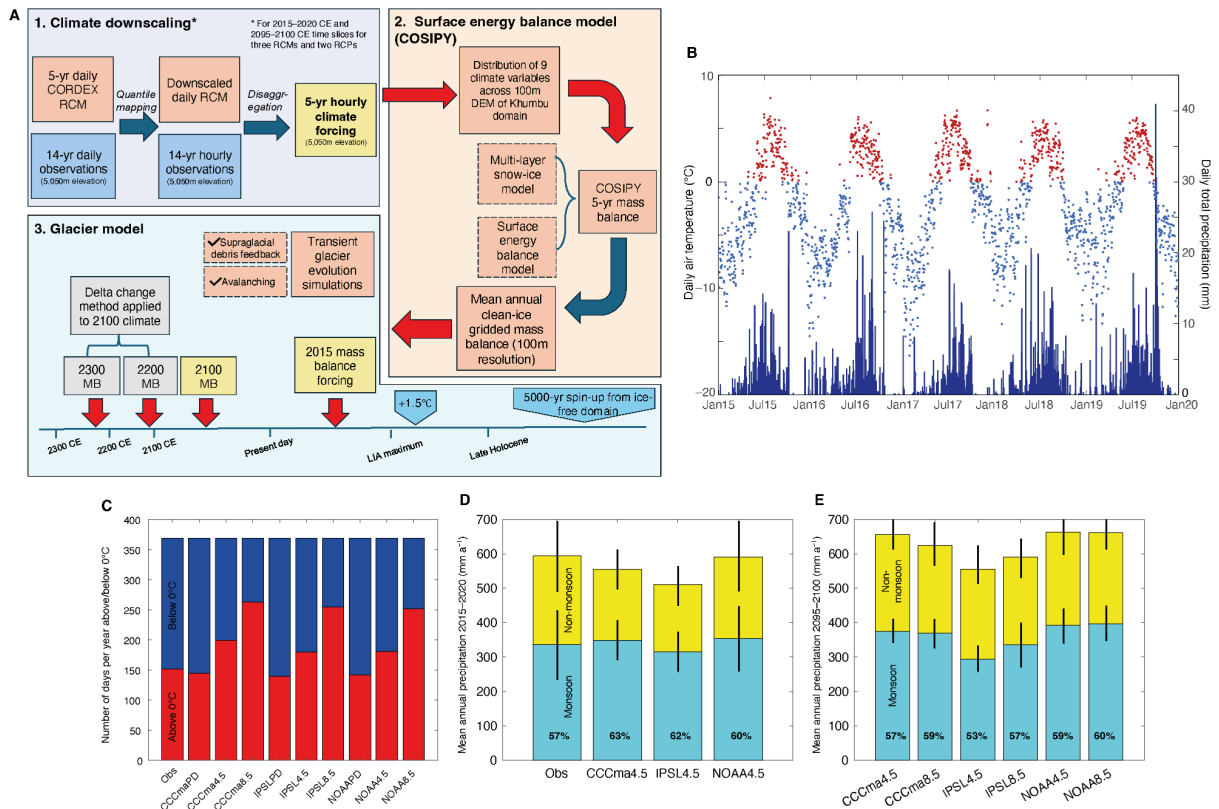
1155
1156
1157

Figures and captions



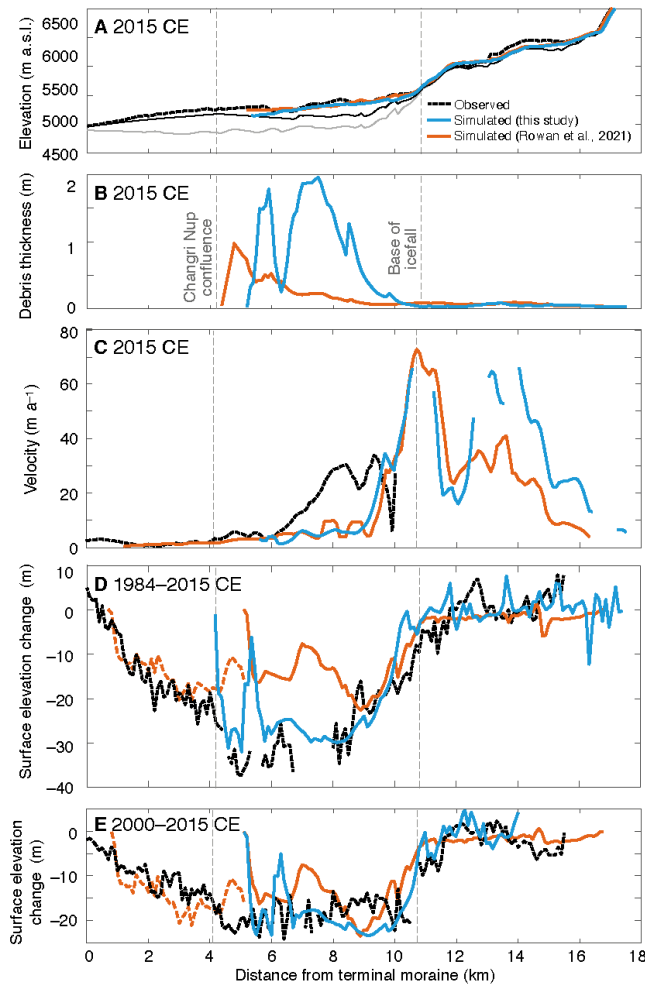
1158
1159
1160
1161
1162
1163
1164
1165
1166
1167
1168
1169
1170
1171
1172
1173
1174

Figure 1: Khumbu Glacier location and context. (a) Location map of High Mountain Asia showing the location of the monsoon-influenced Central and Eastern Himalaya and Khumbu Glacier. (b) hypsometry of glaciers and debris-covered glacier ice in the Central and Eastern Himalaya compared with the elevations of Khumbu Glacier. (c) Satellite image of Khumbu Glacier showing the glacier outline from the RGI database (black line) that is equivalent to the late Holocene (~1 ka) glacier extent identified from ice-marginal moraines, the extent of supraglacial debris, location of the Khumbu Icefall, the extent of active ice flow inferred from observations of glacier velocity, and location of the automatic weather stations used for RCM downscaling (blue stars). (d) Estimated mass balance gradient for debris-covered glaciers in the Everest region (Benn and Lehmkuhl, 2000) compared with the glacier mass balance gradient simulated using the NOAA RCM and showing change in the equilibrium line altitude (ELA) of Khumbu Glacier in the historical and future simulations for the NOAA RCM RCP4.5 experiment.



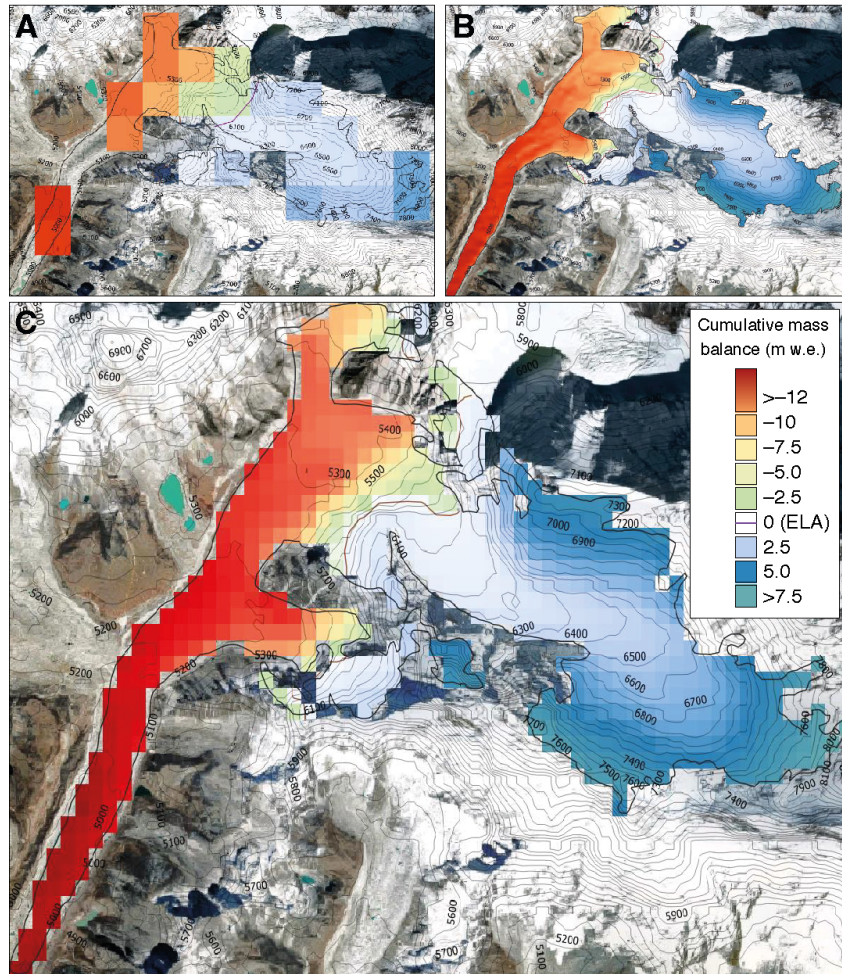
1175
1176
1177
1178
1179
1180
1181
1182
1183
1184
1185
1186
1187
1188
1189
1190
1191
1192
1193
1194
1195
1196
1197
1198

Figure 2: Glacier model experimental design and evaluation of RCM downscaling. (a) Schematic diagram of the glacier modelling approach showing the methods used for downscaling through quantile mapping and disaggregation of climate data. Note that this process does not apply to the post-2100 CE climate forcings which are subject to delta change. Surface energy balance modelling using COSIPY includes the pre-processing stage of meteorological distribution across the Khumbu domain, which is repeated for each RCM in the 2015–2020 CE climates and for the three RCMs and two RCPs for the 2095–2100 CE climates. The simulated mass balance is then used to force the glacier evolution model. (b) Daily mean temperature and daily total precipitation from the NOAA RCM for the present day (2015–2020 CE) following downscaling using quantile mapping with air temperature categorised into above freezing (red) and below freezing (blue). (c) Proportion of air temperatures above and below freezing for the present day for each RCM and RCP for the downscaled daily data compared with observations. (d) Annual precipitation totals for non-monsoon and monsoon with standard deviation between selected years shown by black bars for the downscaled daily data compared with observations. (e) Future (2095–2100 CE) time-slice annual precipitation totals for non-monsoon and monsoon months with standard deviation between selected years shown by black bars. In (d) and (e) the percentage of the total annual precipitation occurring during the monsoon is indicated by the value in bold text. (Obs = meteorological observations from AWS).



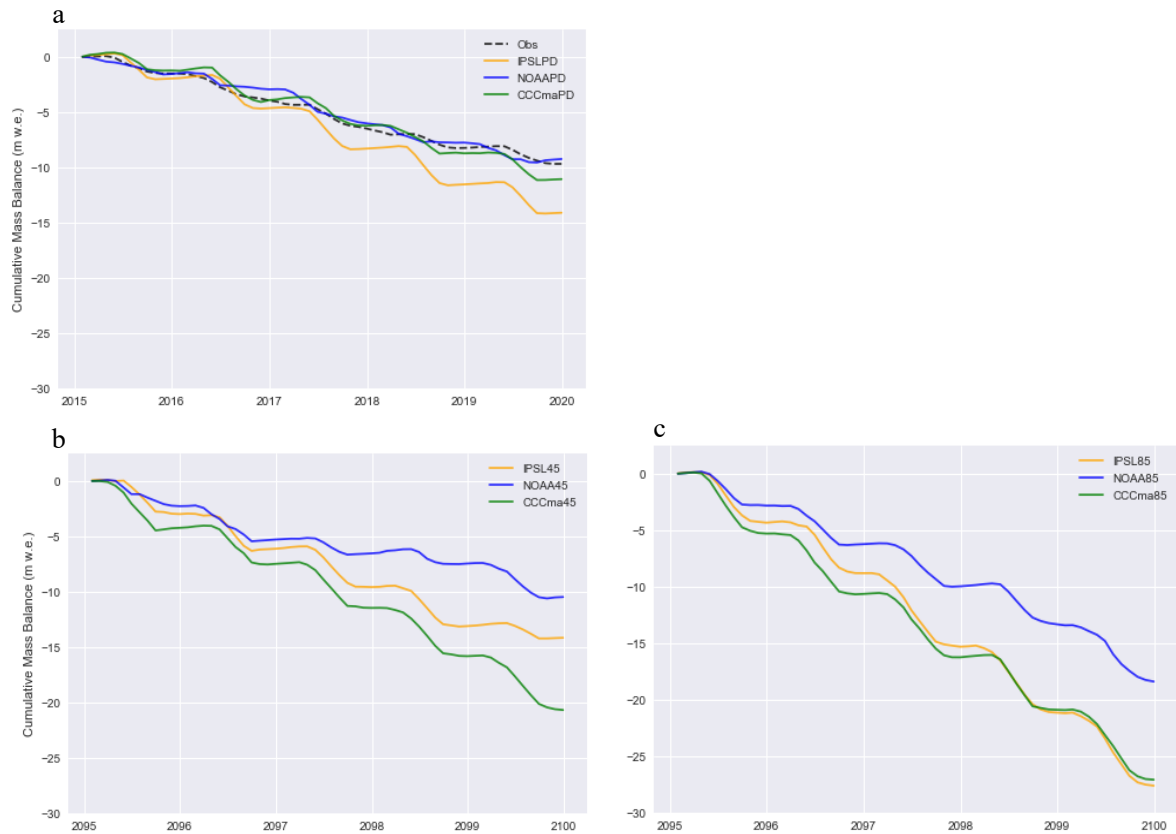
1199
 1200
 1201
 1202
 1203
 1204
 1205
 1206
 1207
 1208
 1209
 1210
 1211
 1212

Figure 3. Evaluation of present-day simulation showing; (a) mean simulated glacier surface elevation and bed elevation calculated from a 500 m-wide swath profile along the central flowline of the glacier. Subglacial topography including the dynamically detached debris-covered tongue is shown by the solid black line and subglacial topography used in the entire glacier simulations in Rowan et al. (2015) is shown for comparison by the lowermost grey solid line. The estimated present-day ice surface elevation (Farinotti et al., 2019) is shown by the dashed black line. (b) mean simulated debris thickness, (c) simulated and observed velocities from the NASA MEaSUREs ITS_LIVE project (Dehecq et al., 2019), and simulated and observed mean surface elevation change between (d) 1984–2015 CE and (e) 2000–2015 CE compared with results from the simulations in this study and those in Rowan et al. (2021) where further information about the model evaluation can be found.



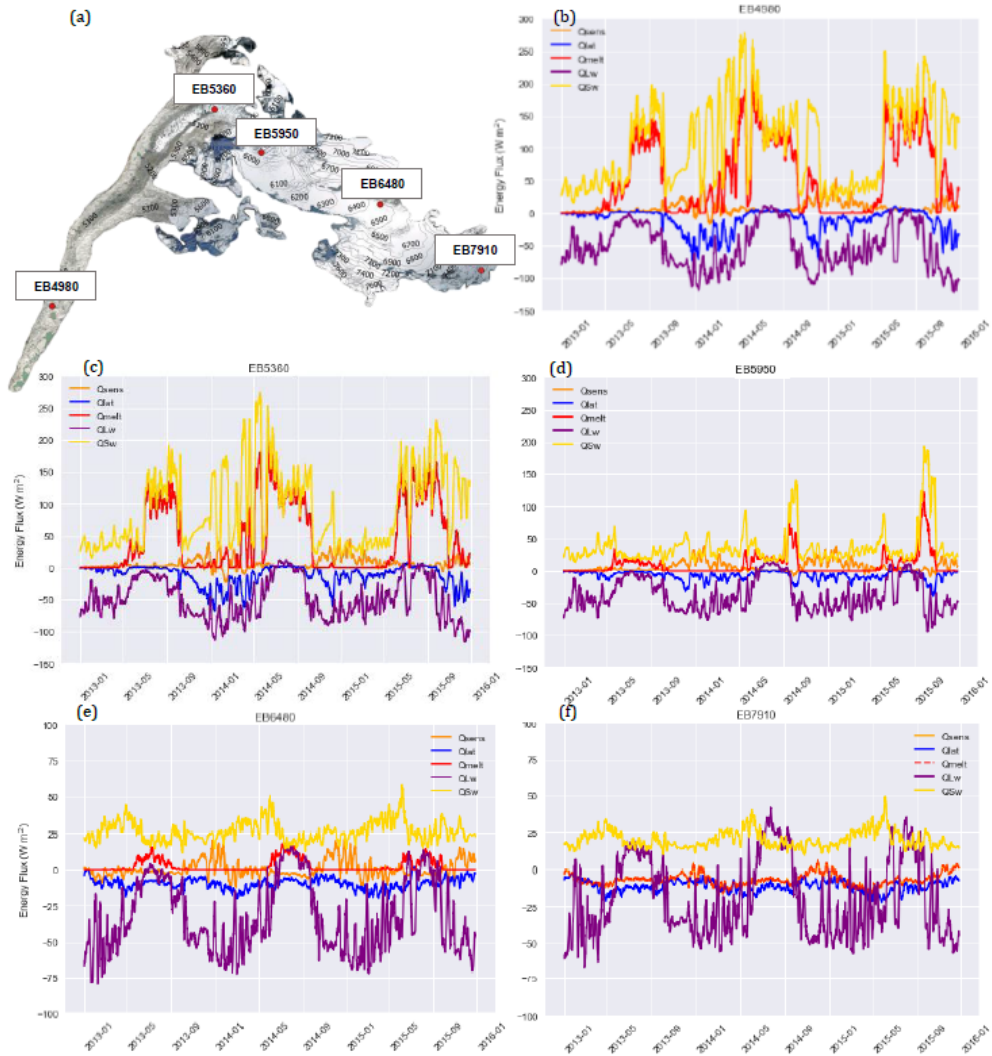
1213
 1214
 1215
 1216
 1217
 1218
 1219

Figure 4. COSIPY reference calculation of present-day mass balance for Khumbu Glacier for the period 2013–2015 CE showing the results from calculations using different grid spacings using (a) a 1-km grid, (b) a 30-m grid, (c) the 200-m grid spacing used throughout the experiments in this study.



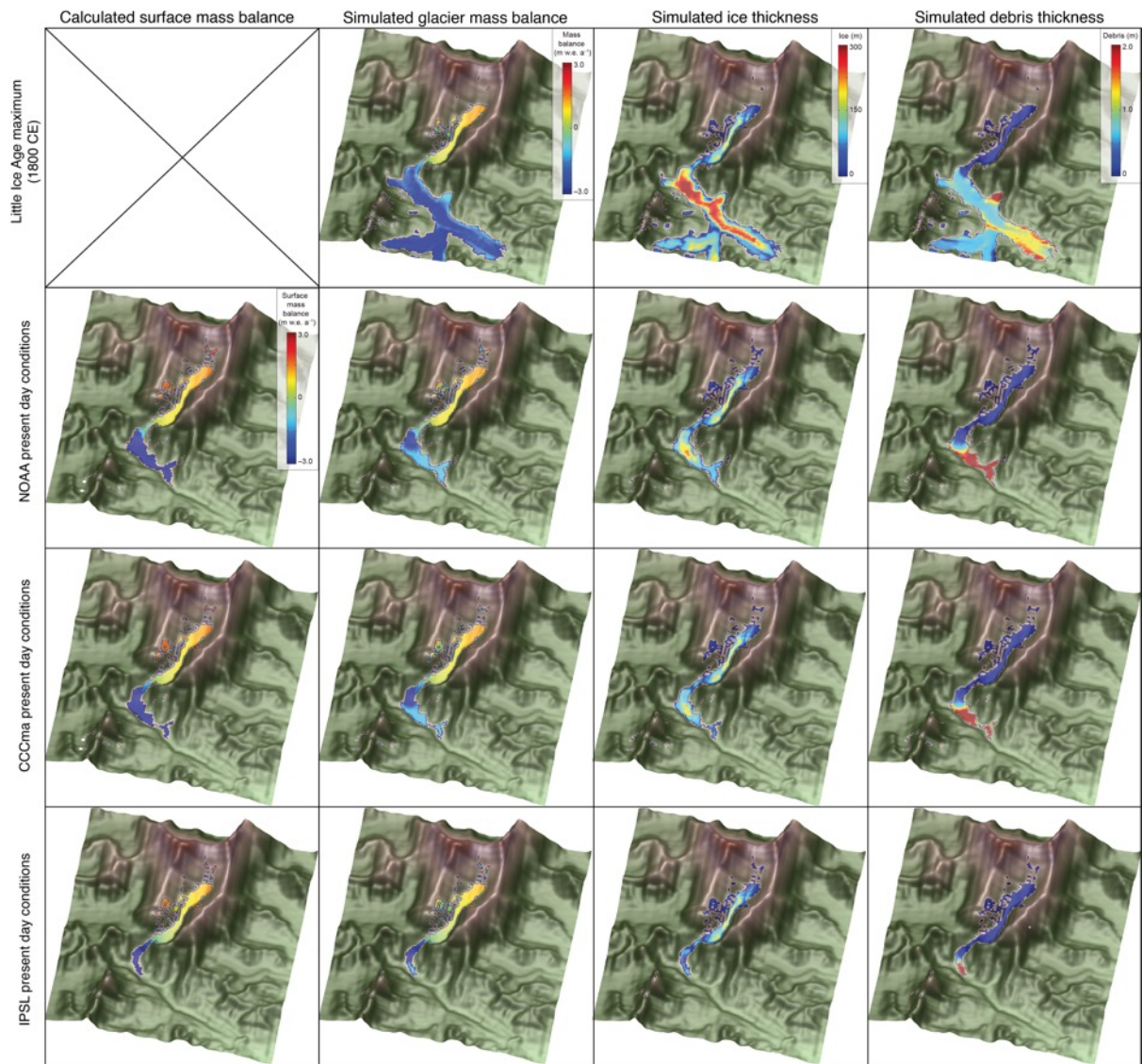
1220
 1221
 1222
 1223
 1224
 1225
 1226
 1227
 1228
 1229
 1230
 1231
 1232
 1233

Figure 5. Spatially averaged cumulative clean-ice mass balance with clear seasonality for (a) the present day time-slice including the mass balance forced by the observations used for downscaling, and the end-of-century time-slice under (b) RCP4.5 and (c) RCP8.5. The low annual glacier-wide mass balance values shown here are the result of the extent of the model domain used to force the glacier model that includes the larger catchment beyond the glacier margins and therefore contains a higher proportion of lower elevations than those of the glacier itself. However the similar mass balance results for simulations forced by NOAA RCM and observations can be clearly seen (a), and the differences between the three RCMs is apparent in all time-slices (a-c).



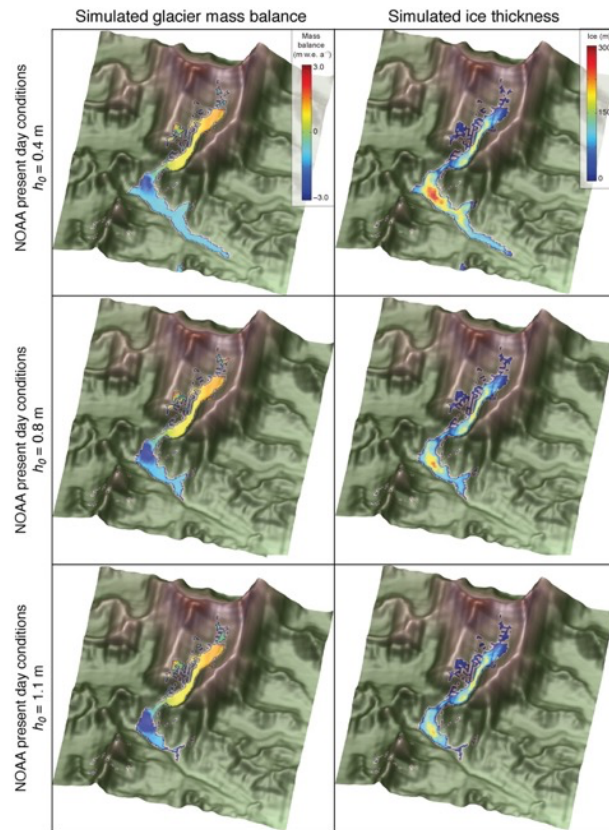
1234
 1235
 1236
 1237
 1238
 1239
 1240
 1241

Figure 6. (a) Locations of energy balance (EB) points used for energy flux and melt components analysis (named after corresponding altitude e.g., EB6480) and (b–f) 5-day average of energy fluxes across study period for each site. Note that scales are different for (e) and (f) compared to (b)–(d) due to the marked difference in absolute values.



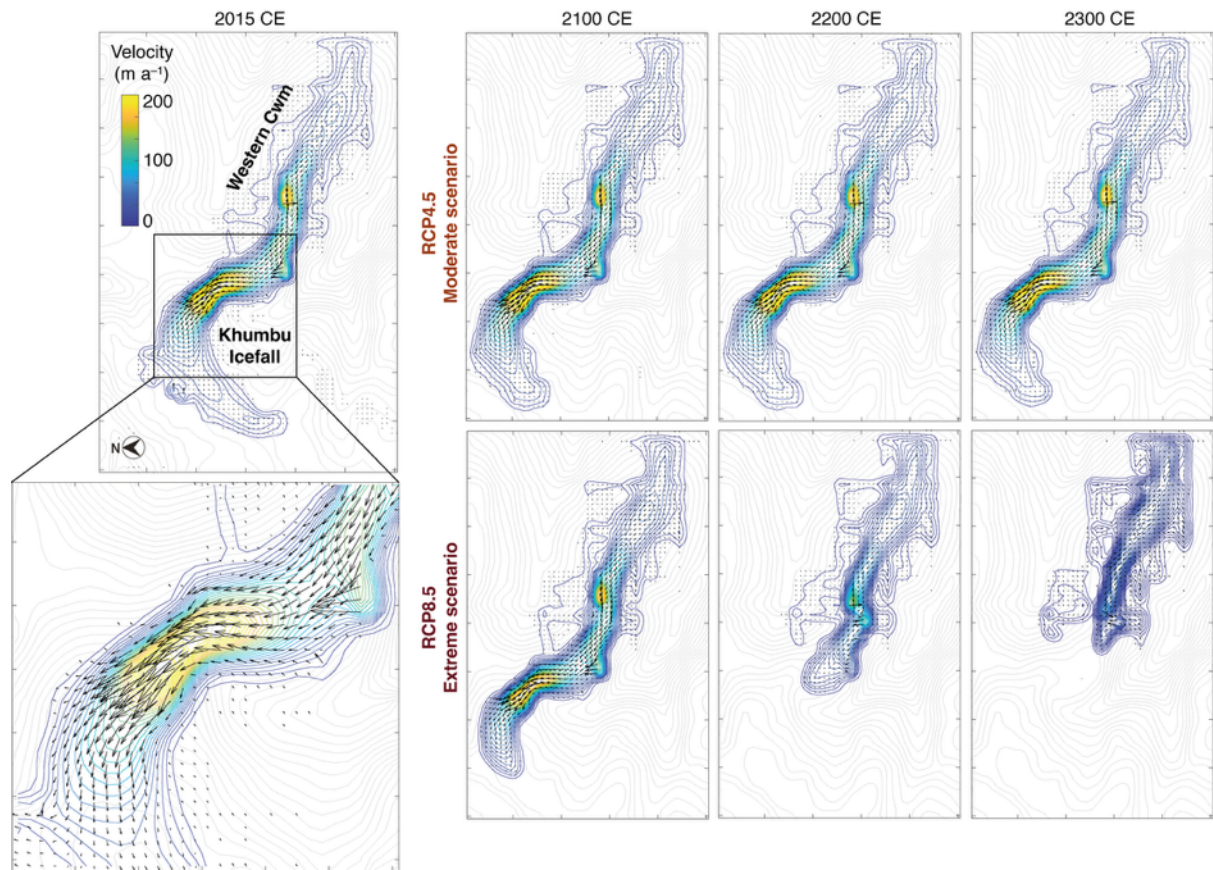
1242
 1243
 1244
 1245
 1246
 1247
 1248
 1249
 1250
 1251
 1252

Figure 7. Glacier model sensitivity to surface energy and mass balance forcing, showing Little Ice Age (~1800 CE) glacier mass balance, ice thickness and debris thickness. Present-day results for surface mass balance calculated using each RCM with COSIPY showing glacier mass balance calculated using the same climate forcing following integration with the glacier model, simulated ice thickness, and simulated debris thickness.



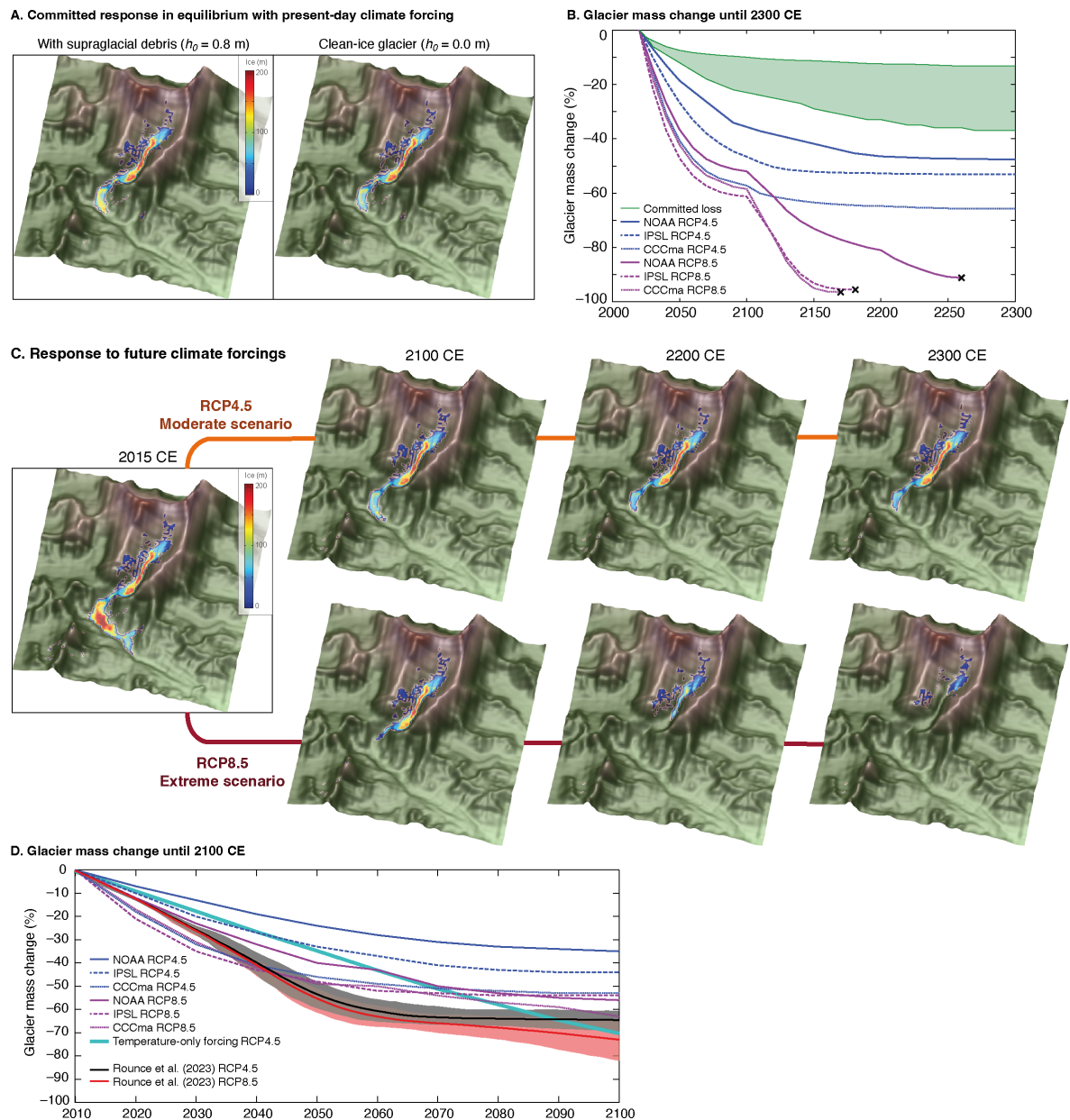
1253
 1254
 1255
 1256
 1257
 1258
 1259
 1260
 1261
 1262

Figure 8. Glacier mass balance and ice thickness simulated using the NOAA RCM climate forcing and the resulting simulated ice thickness for h_0 values of 0.4 m, 0.8 m, and 1.1 m where h_0 is a constant in Equation(1) representing the characteristic debris thickness at which the reduction in ablation due to insulation by supraglacial debris is 50% of the value for an equivalent clean-ice surface (Anderson and Anderson, 2016; Rowan et al., 2021).



1263
 1264
 1265
 1266
 1267
 1268
 1269
 1270
 1271
 1272
 1273

Figure 9. Simulated ice flow for Khumbu Glacier. Velocity-vector maps showing simulated ice flow magnitude and direction from the present day (2015–2020 CE) until 2300 CE under RCP4.5 and RCP8.5 using the downscaled NOAA climate forcing. Simulated ice flow speed is shown as colour shading with blue contours, and the bed topography is shown by grey contours. The outermost contour in each plot represents the slowest ice flow close to the glacier margins with depth-integrated velocities of 5–10 m a⁻¹. Note that rapid flow across the Western Cwm indicated by one arrow shows the effects of avalanching rather than sustained glacier flow.



1274
 1275
 1276
 1277
 1278
 1279
 1280
 1281
 1282
 1283
 1284
 1285
 1286
 1287
 1288
 1289
 1290
 1291

Figure 10. Future glacier volume change projections. (a) Equilibrium ice thickness accounting for the committed response to recent climate change using the downscaled NOAA RCM climate forcing with and without the effect of supraglacial debris on mass balance. (b) Simulated glacier volume change from the present day (2015–2020 CE) until 2300 CE under RCP4.5 and RCP8.5 for the three downscaled RCMs. The black crosses mark when ice flow has declined sufficiently that the glacier is considered almost absent or no longer viable. The green shading shows the range of the committed volume loss due to historical warming. (c) Simulated ice thickness under RCP4.5 and RCP8.5 for 2100 CE, 2200 CE and 2300 CE using the downscaled NOAA RCM climate forcing. (d) Comparison of projected shrinkage of Khumbu Glacier by 2100 CE from this study with those from Rounce et al. (2023) showing results from each of the six experiments in this study with results from RCP4.5 and RCP8.5 from Rounce et al. (2023), the equivalent result for a simulation using a change in MAAT equivalent to the NOAA RCP4.5 forcing where precipitation does not change from the present-day value (cyan line).

1292 **Appendix A: Climate Model Downscaling**

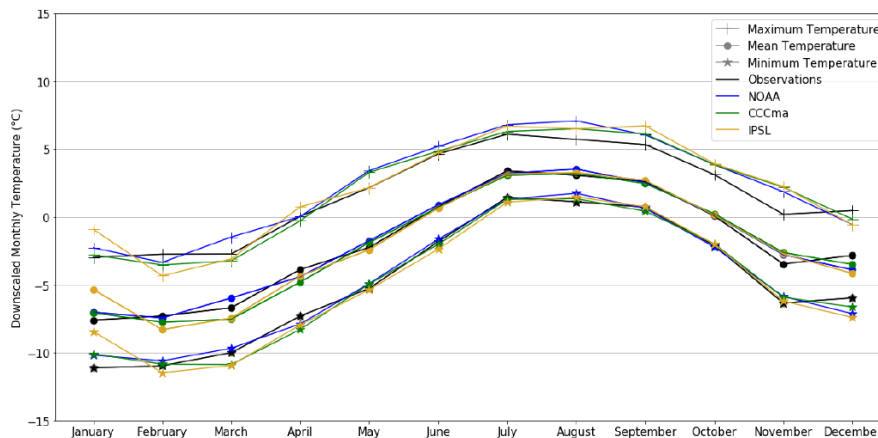
1293 This section contains further details on the RCM downscaling, evaluation of the present-day
1294 downscaled RCM results using meteorological data, and the distribution of these results across the
1295 model domain.

1296
1297 **A1. Meteorological data collection and analysis**

1298 14 years of meteorological observations were collected from two AWS at the Pyramid Observatory at
1299 5,050 m a.s.l. and 5,035 m a.s.l. and the West Changri Nup Glacier AWS at 5,363 m a.s.l.. Missing data
1300 were replaced through interpolation with an alternative AWS from this group. Precipitation was
1301 measured at 15-minute intervals using a Geonor T-200BM sensor mounted 1.8 m above the surface.
1302 Evaporation from the bucket is supposedly blocked by a layer of oil but some does occur as evidenced
1303 by precipitation values below 0 mm. Noise from wind and evaporation were corrected for by
1304 compensating any negative change over the 15-minute time step with the neighbouring positive value
1305 such that accumulated precipitation was unchanged. Periods with prolonged evaporation were set to
1306 zero. Undercatch of snowfall by rainfall gauges was corrected through precipitation phase partitioning
1307 using wind speed observations (Wagnon et al., 2009). For interpolation of air temperature, hourly lapse
1308 rates were used that averaged 5.54 °C km⁻¹ to adjust to the height of the reference point at 5,050 m a.s.l..
1309 Where possible, precipitation data taken from the Pyramid AWS at 5,035 m a.s.l. because this
1310 precipitation gauge provides a longer period of continuous observations than the other gauges and
1311 avoids errors due to low precipitation amounts measured by tipping bucket gauges, which are known
1312 to systematically underestimate snowfall particularly during high winds (Sherpa et al., 2017).

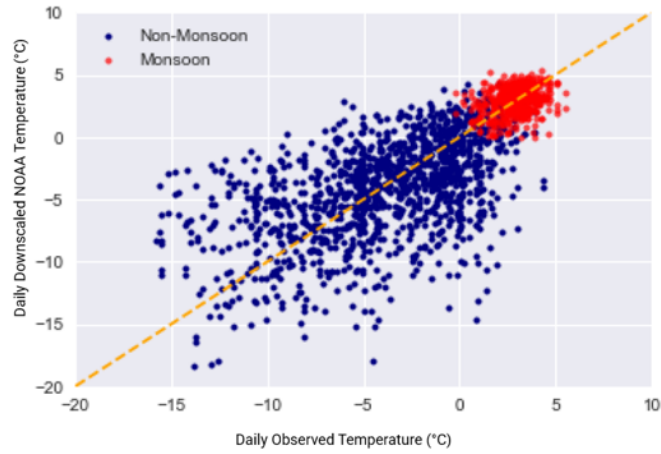
1313
1314
1315 **A1. Downscaled climate model results**

1316
1317



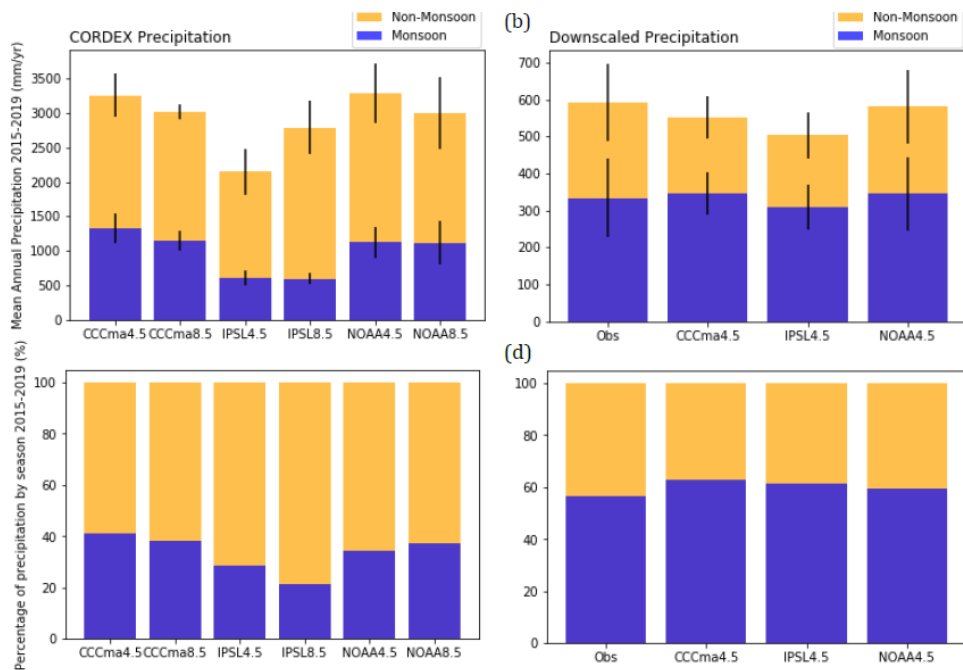
1318
1319
1320
1321
1322
1323
1324
1325
1326

Figure A1: Downscaled monthly mean, maximum, and minimum temperature calculated for the present day time slice.



1327
1328
1329
1330
1331
1332
1333
1334
1335

Figure A2: Daily downscaled temperature from the NOAA RCM against observations, split by monsoon/non-monsoon with a 1:1 line to aid analysis of the temperature distributions (dashed orange line).



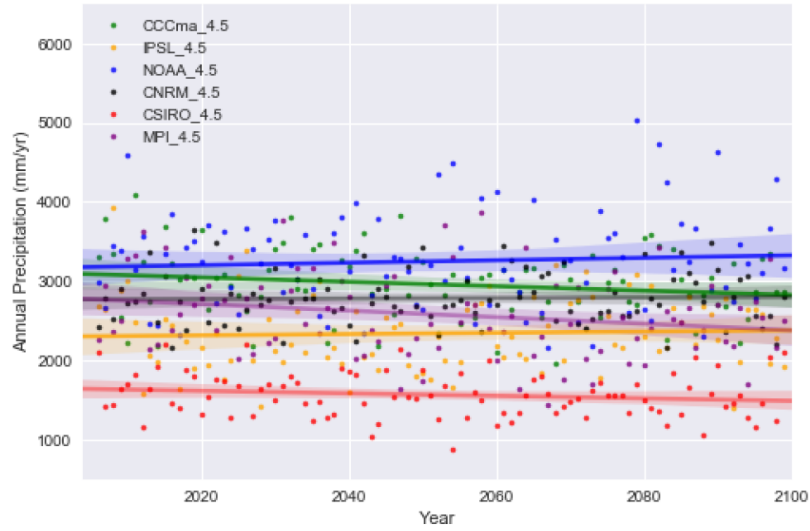
1336
1337
1338
1339
1340
1341
1342
1343
1344

Figure A3. Annual precipitation totals for non-monsoon and monsoon months before and after downscaling with standard deviation between selected years shown by black bars (a and b) and as their seasonal percentages (c and d). The annual precipitation matches measurements in the southern Dudh Koshi catchment for the gridbox nearest to Khumbu Glacier is located at 27.9065056°N, 86.4352951°E which is 2,100 m a.s.l..

A2. Regional Climate Model analysis and selection

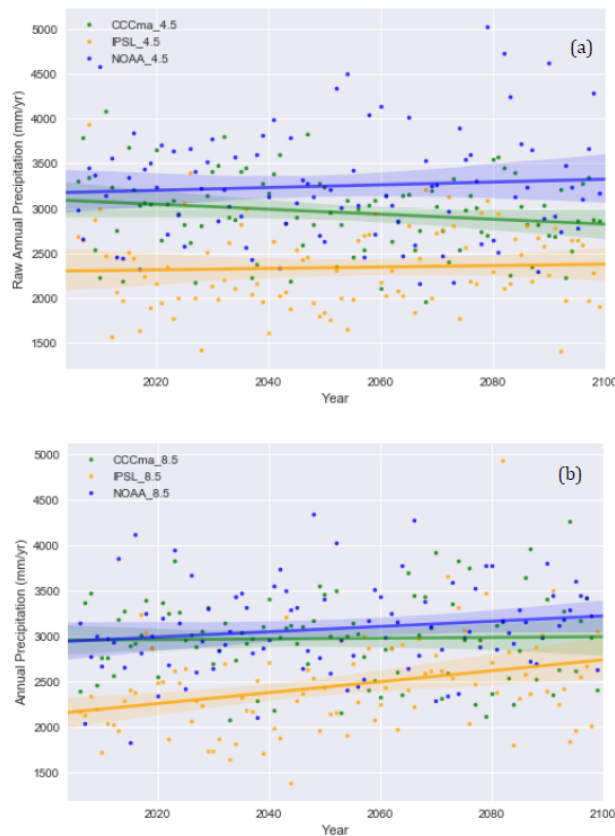
1346 Three of the six available CORDEX South Asia RCMs (NOAA, CCCma, IPSL) were selected as
1347 discrete scenarios that span the range of possible future precipitation conditions (Table 1); either wet,
1348 moderate, or dry climate in 2080–2100 CE (Figure A4). The raw RCMs significantly overestimate
1349 annual total precipitation by at least a factor of five for the selected gridpoint which is corrected for by
1350 downscaling these results using AWS data.

1351



1352
1353
1354
1355
1356
1357
1358

Figure A4: Annual precipitation sums (dots) with fitted trend line from the start of the RCP experiments (2006) until the end (2100) for each of the six Indian Institute for Tropical Meteorology CORDEX models for RCP4.5.



1359
1360
1361
1362
1363
1364
1365
1366

Figure A5: Annual precipitation sums (dots) with fitted trend line from the start of the RCP experiments (2006) until the end (2100) for the three selected of the six CORDEX models for RCP4.5 (a) and 8.5 (b).

1367 **A3. Downscaling parameters and method**

1368 Though minimum and maximum temperature are not required to force COSIPY, these were downloaded
 1369 and statistically downscaled using QM with normal distribution to aid disaggregation to an hourly time
 1370 step using MELODIST. Quantile mapping for the CORDEX wind speed data was found to be
 1371 ineffective when analysing the time series output against observations, both for the absolute wind speed
 1372 as well as the reduced day-on-day variability seen during the monsoon. Therefore, GARD was used
 1373 instead. This is a simple statistical analogue regression downscaling method appropriate for pointwise
 1374 downscaling.

1375
 1376

1377 Table A1: RCM-derived parameters and the method used for downscaling or bias correction.

RCM-derived parameters	Downscaling/bias correction method	Parametric distribution model (for QM)	References
Precipitation (kg per m ² per s, converted to mm day ⁻¹)	Quantile mapping (QM)	Gamma	Vrac et al., 2007; Piani et al., 2010
Mean temperature (K) Minimum temperature (K) Maximum temperature (K)	QM	Normal / Gaussian	Li et al., 2010, Gupta et al., 2016; Luo et al., 2018
Incoming shortwave (W m ⁻²) Incoming longwave (W m ⁻²) Relative humidity (%)	QM	Beta	Ruane et al., 2015
Pressure (hPa)	Bias correction	N/A	N/A
Wind speed (m s ⁻¹)	Regression downscaling	N/A	Gutmann et al., 2022

1378
 1379

1380 **A4. Meteorological distribution across the model domain**

1381 Temperature and precipitation were interpolated across the 100-m DEM using a linear relationships:

1382
 1383

$$V_{interp} = (V) + (Z_{pixel} - Z_{station}) \cdot LR$$

1384
 1385

1385 where V_{interp} is the variable to be interpolated, V is the hourly variable in question (e.g. temperature or
 1386 precipitation), Z_{pixel} is the elevation (m a.s.l.) of the target pixel in the domain, $Z_{station}$ the elevation (m)
 1387 of the station, and LR is the lapse rate for temperature or gradient for precipitation calculated from
 1388 meteorological observations, as described below. Note that the distribution is from a prescribed
 1389 elevation, not from the exact location of the AWS.

1390
 1391

1391 The mass balance sensitivity to lapse rate that differed depending on season or time of day were
 1392 examined, showing a lesser impact on glacier-wide mass balance than in other studies due to the large
 1393 elevation range of Khumbu Glacier where a smaller fraction of the glacier relative to total area is located
 1394 along the zero degree isotherm (*cf.* Yala Glacier; Immerzeel et al., 2014). Lapse rates that changed
 1395 depending on season and time of day (given marked monsoonal and nocturnal lowering of lapse rates)
 1396 averaging 5.54 °C km⁻¹ were calculated and, following integration with the glacier model, produced
 1397 glacier-wide mass balance and spatial calculations that were closest to those from geodetic observations,
 1398 including maximum rates of surface lowering in the upper ablation area where the debris layer is
 1399 thinnest (King et al., 2020) (Fig. 1d).

1400
 1401

1401 Analysis of meteorological observations made between 2,600 m and 5,600 m a.s.l. from the Ev-K2-
 1402 CNR and Glacioclim networks indicated that precipitation gradients were weak, slightly negative or
 1403 absent across the Dudh Koshi catchment, confirming the observations of Salerno et al. (2015) and Yang
 1404 et al. (2017). Given the high incidence of missing precipitation data from high-elevation AWS, the
 1405 undercatch of snow associated with tipping bucket rain gauges, and the absence of precipitation
 1406 measurements above 5,600 m a.s.l. precipitation was not varied with elevation. To test the sensitivity
 1407 of precipitation to elevation, COSIPY was forced by a gridded climate distributed using weak negative,
 1408 weak positive, and no precipitation gradients. The results of these experiments were used to force the

1409 glacier model, and the simulated historical glacier evolution was similar, with only a 10 m difference
1410 in the maximum ice thickness between simulations with different precipitation gradients.

1411
1412 Direct solar radiation across the model domain was corrected by the slope, azimuth, and shadowing
1413 potential of each pixel (Wohlfahrt et al., 2016; Sauter et al., 2020). A footprint-weighted correction was
1414 also applied to horizontal measurements of net radiation. The fraction of diffuse incoming shortwave
1415 radiation was estimated by using the ratio of total shortwave (global) radiation and potential shortwave
1416 radiation to define a clearness index (Wohlfahrt et al., 2016). This clearness index was used to calculate
1417 diffuse radiation, which is calibrated with data from Neustift, an eddy covariance station in the Austrian
1418 Alps (Wohlfahrt et al., 2008). The distributed radiative fluxes were compared with high-elevation
1419 stations for 2019 to assess the efficacy of this method across the domain. Pressure was distributed across
1420 the domain by first calculating sea level pressure (*cf.* Lente and Osz, 2020) and then interpolated with
1421 the barometric equation. The relative humidity gradient was calculated as $-0.002\% \text{ m}^{-1}$ from Ev-K2-
1422 CNR and Glacioclim networks and validated with National Geographic network to capture trends at
1423 higher elevations (Matthews et al., 2020). Wind speed was assumed to be uniform across the domain.

1424
1425

1426 **Additional references for Appendix A**

1427 Gupta, A. and Tarboton, D.G. 2016. A tool for downscaling weather data from large-grid reanalysis
1428 products to finer spatial scales for distributed hydrological applications. *Environmental*
1429 *Modelling & Software*. 84, pp. 50–69. <https://doi.org/10.1016/j.envsoft.2016.06.014>

1430 Gutmann, E. D., J. J. Hamman, M. P. Clark, T. Eidhammer, A. W. Wood, and J. R. Arnold, 2022: En-
1431 GARD: A Statistical Downscaling Framework to Produce and Test Large Ensembles of Climate
1432 Projections. *J. Hydrometeor.*, 23, 13545–1561, <https://doi.org/10.1175/JHM-D-21-0142.1>.

1433 Immerzeel, W., Petersen, L., Ragetti, S. and Pellicciotti, F. 2014. The importance of observed gradients
1434 of air temperature and precipitation for modelling runoff from a glacierized watershed in the
1435 Nepalese Himalayas. *Water Resources Research*. 50: 2212-2226. doi: 10.1002/2013WR014506.

1436 Lente, G. and Ösz, K., 2020. Barometric formulas: various derivations and comparisons to
1437 environmentally relevant observations. *ChemTexts*, 6, pp.1-14. [https://doi.org/10.1007/s40828-](https://doi.org/10.1007/s40828-020-0111-6)
1438 [020-0111-6](https://doi.org/10.1007/s40828-020-0111-6)

1439 Li, H., Sheffield, J. and Wood, E.F., 2010. Bias correction of monthly precipitation and temperature
1440 fields from Intergovernmental Panel on Climate Change AR4 models using equidistant quantile
1441 matching. *Journal of Geophysical Research: Atmospheres*, 115(D10).
1442 <https://doi.org/10.1029/2009JD012882>

1443 Ruane, A. C., Goldberg, R., and Chryssanthacopoulos, J. 2015. Climate forcing datasets for agricultural
1444 modeling: Merged products for gap-filling and historical climate series estimation, *Agricultural*
1445 *and Forest Meteorology*, 200, pp. 233–248. <https://doi.org/10.1016/j.agrformet.2014.09.016>

1446 Salerno, F., Guyennon, N., Thakuri, S., Viviano, G., Romano, E., Vuillermoz, E., Cristofanelli, P.,
1447 Stocchi, P., Agrillo, G., Ma, Y., and Tartari, G. (2015). Weak precipitation, warm winters and
1448 springs impact glaciers of south slopes of Mt. Everest (central Himalaya) in the last 2 decades
1449 (1994–2013), *The Cryosphere*. 9: 1229-1247. doi: 10.5194/tc-9-1229-2015.

1450 Vrac, M., Stein, M.L., Hayhoe, K. and Liang, X.Z., 2007. A general method for validating statistical
1451 downscaling methods under future climate change. *Geophysical Research Letters*, 34(18).
1452 <https://doi.org/10.1029/2007GL030295>

1453 Wohlfahrt, G., Hammerle, A., Haslwanter, A., Bahn, M., Tappeiner, U. and Cernusca, A. 2008.
1454 Disentangling leaf area and environmental effects on the response of the Net Ecosystem Co2
1455 Exchange to diffuse radiation, *Geophysical Research Letters*, 35(16).
1456 doi:10.1029/2008gl035090.

1457 Wohlfahrt, G., Hammerle, A., Niedrist, G., Scholz, K., Tomelleri, E. and Zhao, P. 2016. On the energy
1458 balance closure and net radiation in complex terrain, *Agricultural and Forest Meteorology*, 226–
1459 227, pp. 37–49. doi:10.1016/j.agrformet.2016.05.012.

1460 Yang, K., N. Guyennon, L. Ouyang, L. Tian, G. Tartari, and F. Salerno (2017). Impact of summer
1461 monsoon on the elevation-dependence of meteorological variables in the south of Central
1462 Himalaya. *International Journal of Climatology*. 5293: 1748-1759. doi:10.1002/joc.5293.